Published in final edited form as:

Nat Aging. 2021 October ; 1(10): 962–973. doi:10.1038/s43587-021-00107-6.

An inducible *p21*-Cre mouse model to monitor and manipulate *p21*-highly-expressing senescent cells *in vivo*

Binsheng Wang[1,2,9], **Lichao Wang**[1,2,9], **Nathan S. Gasek**[1,2,9], **Yueying Zhou**[3,4], **Taewan Kim**[1,2,5], **Chun Guo**[1], **Evan R. Jellison**[6], **Laura Haynes**[1,6], **Sumit Yadav**[7], **Tamar Tchkonia**[8], **George A. Kuchel**[1], **James L. Kirkland**[8], **Ming Xu**[1,2,10]

[1]UConn Center on Aging, UConn Health, Farmington, CT

[2]Department of Genetics and Genome Sciences, UConn Health, Farmington, CT

[3]Xiangya Stomatological Hospital, Central South University, Changsha, China

[4]Center for Regenerative Medicine and Skeletal Development, UConn Health, Farmington, CT

[5]Biomedical Science Graduate Program, UConn Health, Farmington, CT

[6]Department of Immunology, UConn Health, Farmington, CT

[7]Division of Orthodontics, UConn Health, Farmington, CT

[8]Robert and Arlene Kogod Center on Aging, Mayo Clinic, Rochester, MN

[9]These authors contributed equally

Abstract

The role of senescent cells has been implicated in various tissue dysfunction associated with aging, obesity, and other pathological conditions. Currently, most transgenic mouse models only target *p16*^{Ink4a}-highly-expressing (*p16*^{high}) cells. Here, we generated a *p21*-Cre mouse model, containing a *p21* promoter driving inducible Cre, enabling us to examine *p21*^{Cip1}-highly-expressing (*p21*^{high}) cells, a previously unexplored cell population exhibiting several characteristics typical of senescent cells. By crossing *p21*-Cre mice with different floxed mice, we managed to monitor, sort, image, eliminate, or modulate *p21*^{high} cells *in vivo*. We showed *p21*^{high} cells can be induced by various conditions, and percentages of *p21*^{high} cells varied from 1.5 to 10% across different tissues in 23-month-old mice. Intermittent clearance of *p21*^{high} cells improved physical function in 23-month-old mice. Our study demonstrates that the *p21*-Cre mouse model is a valuable and powerful tool for studying *p21*^{high} cells to further understand the biology of senescent cells.

[10]Correspondence should be addressed to: M.X. (mixu@uchc.edu).

Author Contributions

M.X., J.L.K., and T.T. conceived *p21*-Cre mouse model. M.X. designed, generated, and validated the *p21*-Cre mouse model. B.W., L.W., N.S.G., Y.Z., C.G., T.K., and M.X. performed the mouse studies. B.W. and E.R.J. contributed to the FACS analysis. N.S.G., B.W., and Y.Z. contributed to the histological analysis. L.H., S.Y., G.A.K., and J.L.K. contributed to manuscript preparation. M.X. wrote the manuscript with input from all coauthors. M.X. oversaw all experiments, data analysis, and manuscript preparation.

Competing Interests

None of the authors have competing financial or non-financial interests.

Peer review Information:

Nature Aging thanks Valery Krizhanovsky, and the other, anonymous reviewer(s) for their contribution to the peer review of this work.

Editor summary:

Wang et al, report a mouse model which can target p21-highly-expressing senescent cells. Using this model, they are able to monitor, sort, image, eliminate, or modulate these cells in vivo, which could be a valuable tool to study senescent cells.

Introduction

Cellular senescence is a cell fate characterized by essentially irreversible proliferative arrest[1]. A variety of stimuli, including DNA damage, dysfunctional telomeres, oncogenic proteins, fatty acids, reactive oxygen species (ROS), mitogens, and cytokines, can act alone or in combination to drive cells into the cellular senescence fate through pathways involving *p16*/*Rb* (retinoblastoma), *p53*/*p21*, and probably others[2]. These contribute to the widespread changes in gene expression that underlie senescence-associated growth arrest, the senescence-associated secretory phenotype (SASP), resistance to apoptosis, and changes in morphology[2,3]. In these respects, cellular senescence can be considered a state of major cellular programming in addition to differentiation, proliferation, or apoptosis. Intracellular autocrine loops reinforce progression to irreversible replicative arrest, heterochromatin formation, and initiation of the pro-inflammatory SASP over a span of days to weeks[2,4].

Senescent cell burden increases in various tissues with aging[5] and multiple chronic conditions[6]. Depending on specific tissues and varied pathological states, the percent of senescent cells can vary from 1-20%[7–9]. In spite of relatively small percentages, senescent cells cause substantial tissue dysfunction[10]. Senescent cells can elicit damage in both an autocrine and paracrine fashion. In addition to intracellular dysfunction induced by autocrine signaling, senescent cells can be “contagious” and induce cellular senescence and the SASP in nearby non-senescent cells[9,11–14]. Senescent cells can also directly impair function of healthy stem cells[8]. The paracrine signaling from senescent cells, possibly through the SASP, ROS, or other factors, amplifies damage within tissues, which might partially explain why small number of senescent cells can be so harmful.

Currently, the *INK-ATTAC*[15] and *p16-3MR*[16] mouse models are the two most commonly used transgenic models to investigate the role of senescent cells *in vivo*. Both models were designed using the *p16* promoter to drive an inducible suicide gene, by which $p16^{Ink4a}$-highly-expressing ($p16^{high}$ cells) can be eliminated *in vivo*. By leveraging these two models, the causal role of $p16^{high}$ cells has been suggested in a number of pathological conditions including osteoporosis[17], metabolic dysfunction[8,18], osteoarthritis[19], neurodegenerative diseases[20], cardiac dysfunction[7], kidney dysfunction[7], vasomotor dysfunction[21], atherosclerosis[22], liver steatosis[23], pulmonary fibrosis[24], stem cell dysfunction[8,25], and lifespan reduction[7]. Recently, two more senescence-related transgenic mouse models were reported[26,27], both of which had knock-in Cre inserted into the native *p16* locus. Although valuable, all of these models only target $p16^{high}$ cells. Since not all $p16^{high}$ cells are senescent[28,29], and not all senescent cells express high levels of $p16^{1}$, it has been increasingly perceived by the field that *p16* might not be a fully sensitive or specific marker for senescent cells. Models that target other cellular senescence markers are needed

to expand our understanding of the underlying complexity and heterogeneity of senescence biology especially when studied *in vivo*.

p16 and $p21^{Cip1}$ (*p21*) are two major regulators, as well as being the two most recognized and used cellular markers for senescent cells[30]. However, unlike $p16^{high}$ cells, the role of *p21*-highly-expressing ($p21^{high}$) cells *in vivo* remains largely unknown at this time. In this study, we generated a *p21*-Cre transgenic mouse model containing a *p21* promoter driving an inducible Cre, allowing us to investigate $p21^{high}$ cells *in vivo*. By crossing this model with floxed mouse models, we were able to monitor, image, sort, eliminate, and modulate $p21^{high}$ cells *in vivo*. The *p21*-Cre mouse model holds great promise as a valuable and potentially powerful tool for examining the role and underlying mechanisms of $p21^{high}$ cells in aging and in various diseased conditions associated with cellular senescence.

Results

$p16^{high}$ and $p21^{high}$ cells are two distinct cell populations.

Senescent cells are highly heterogeneous in their biological properties, tissue distribution and responses to varied therapies[31]. Although *p16* and *p21* have been widely used as two major cellular markers for senescent cells, very little is known about possible overlap of $p16^{high}$ cells and $p21^{high}$ cells or their respective population diversity. To explore this, we leveraged a single cell transcriptomic (SCT) atlas database, *Tabula Muris Senis*[32], which includes transcriptomic data from a range of tissues in 18-30 months old mice. We visualized the *p21* and *p16* expression levels using the browser based interactive platform (https://tabula-muris-senis.ds.czbiohub.org/). In aged visceral fat, $p21^{high}$ cells are mainly endothelial cells, mesenchymal stem cells, and myeloid cells, while $p16^{high}$ cells are scarce. In liver, $p21^{high}$ cells are mainly Kupffer cells, and myeloid cells, while $p16^{high}$ cells, are mainly Natural Killer (NK) cells and a different population of Kupffer cells. In heart, $p21^{high}$ cells are mainly endothelial cells, while $p16^{high}$ cells are mainly leukocytes (Extended Data Fig.1). Thus, $p16^{high}$ cells and $p21^{high}$ cells are indeed two distinct populations, at least in aged tissues. These findings emphasize the need for models targeting $p21^{high}$ cells.

Generation of *p21*-Cre mouse model.

To generate the *p21*-Cre mouse model, we synthesized a 7 kb DNA fragment (Fig.1a) containing a 3225 bp mouse *p21* promoter fragment followed by a bicistronic message consisting of the coding sequence for *Cre recombinase* (Cre) fused to a tamoxifen-inducible estrogen receptor (ER^{T2}) domain[33]. Cre-ER^{T2} is normally retained in the cytoplasm (inactive) in the absence of an inducer. Upon addition of tamoxifen or 4-hydroxytamoxifen (4-OHT), the Cre-ER^{T2} translocates to the nucleus where it acts preferentially on *loxP* sites. An internal ribosome entry site (IRES) followed by an open reading frame (ORF) coding for enhanced green fluorescent protein (GFP) was also added to facilitate detection of $p21^{high}$ cells. The 3225 bp mouse *p21* promoter fragment is well conserved between human and mouse, and contains 3 *p53*-binding sites responsive to DNA damage[34]. Integrase-mediated transgenesis (IMT)[35] was used to generate the *p21*-Cre transgenic mice. The synthesized fragment (*p21*-Cre) was first subcloned into the vector pBT378 containing 2 attB sites, then was microinjected into the pronucleus of recipient zygotes containing attP sites in the

Hipp11 (*H11,* chromosome 11) locus, which has a high recombination rate and results in stable expression of a single copy of the transgene[36]. Site-specific recombination occurred between the attB sites in the construct and attP sites in the *H11* genomic locus, leading to insertion of *p21*-Cre transgene into the *H11* locus.

One advantage of this site-specific transgenic approach using the the *H11* locus is that it is far less likely to interfere or disrupt any endogenous gene as opposed to the use of random insertion or insertion into targeting gene locus. In addition, this approach allows us to design genotyping primers to distinguish +/+, *p21*-Cre/+, and *p21*-Cre/*p21*-Cre genotypes (Fig.1b). As shown in Fig.1c, we validated two different sets of genotyping primers. For set 1, SH176-F and SH178-R generated a 326bp band for the wildtype (*WT*) allele, while Cre-F and Cre-R generated a 200bp band for the *p21*-Cre transgene allele. For set 2, SH176-F and SH178-R generated a 326bp band for the *WT* allele while SH176-F and BT436-R generated a 260bp band for the *p21*-Cre transgene allele.

Whole-body live imaging of *p21*^{high} cells *in vivo*.

To validate function of the transgene, we first crossed the *p21*-Cre mouse with floxed knock-in firefly luciferase (**LUC**) mice[37]. Floxed knock-in LUC mice contain a *loxP*-flanked STOP fragment between the *Gt(ROSA)26Sor* (ROSA) promoter and LUC, which prevents LUC expression without presence of Cre (Fig.2a). We generated *p21*-Cre/+; LUC/+ (**PL**) mice (Fig.2a), which contain one copy of *p21*-Cre in chromosome 11 and one copy of LUC in chromosome 6. This PL mouse model allows us to detect *p21*^{high} cells in live mice through bioluminescence imaging (**BLI**) in a temporal manner. Doxorubicin (**DOXO**) is a potent DNA damaging agent, which can induce *p21* expression[38] and accumulation of *p21*^{high} cells. We treated PL mice with DOXO and tested whether we could detect *p21*^{high} cells *in vivo*. We observed little signal in either the DOXO- or PBS-treated groups without tamoxifen treatment (Fig.2b), indicating that Cre or STOP fragment leakage is minimal. After 2 tamoxifen treatments to induce Cre and subsequent LUC activity in *p21*^{high} cells, DOXO-treated PL mice had more BLI signal compared to PBS-treated ones (Fig.2b), suggesting the transgene works properly. Metabolic stress and obesity are also known to induce cellular senescence[13] and *p21* expression[39]. We next examined whether we can detect *p21*^{high} cells in PL mice under metabolic stress. We fed PL mice with a high fat diet (HFD) for 4 months, and then treated these mice with 2 doses of tamoxifen. We found HFD significantly increased BLI signals in PL mice when compared to regular chow diet (RCD), indicating accumulation of *p21*^{high} cells with obesity (Fig.2c). Moreover, we examined whether *p21*^{high} cells are induced with aging. We treated 3-month-old (young) and 23-month-old (old) PL mice with 2 doses of tamoxifen, and found that BLI signals were significantly higher in old PL mice than young mice (Fig.2d). Thus, all 3 conditions (chemotherapy drugs, obesity, and aging) can induce *p21*^{high} cells, which can be monitored by BLI in live mice.

p21^{high} cells accumulate in various tissues with aging.

To image *p21*^{high} cells using fluorescence *in vivo* at the tissue level, we crossed the *p21*-Cre mouse with floxed knock-in tdTomato mice[40], which contain a *loxP*-flanked STOP fragment between the CMV early enhancer/chicken β actin (CAG) promoter and tdTomato (Fig.3a).

We generated *p21*-Cre/+; tdTomato/+ (**PT**) mice (Fig.3a). Compared to the GFP included in the transgene (driven by *p21* promoter), tdTomato (driven by the strong CAG promoter) generates a much brighter red fluorescent signal with less confounding by an autofluorescent background, which makes it highly suitable for *in vivo* fluorescence imaging. We first examined the *p21* protein level in tdTomato+ cells and tdTomato− cells. We found tdTomato+ cells had more p21+ cells and higher *p21* protein level than tdTomato− cells, indicating the enrichment of *p21* expression in tdTomato+ cells (Extended Data Fig.2a–c). We then treated young (3-month-old) and old (23-month-old) PT mice with 2 doses of tamoxifen and collected a number of tissues for fluorescence imaging. Most of the tissues from old PT mice contained more tdTomato+ $p21^{high}$ cells, including visceral fat, brain, intestine, heart, liver, and skeletal muscle (Fig.3b). The percentages of $p21^{high}$ cells in these old tissues ranged from 1.5 to 10%, comparable to the percent of senescent cells in aged tissues. No reliably tdTomato+ cells were seen in aged kidneys due to high autofluorescence, and very few tdTomato+ cells were observed in the aged lung. Importantly, very few tdTomato+ cells were seen in all the tissues we collected from young and healthy PT mice, indicating that our *p21*-Cre mouse model might only target age- or disease-specific cells such as senescent cells without affecting most cells in young mice. $p21^{high}$ cells can also be detected by flow cytometry. Consistent with the fluorescence imaging, flow cytometry analysis revealed that the tdTomato+ $p21^{high}$ cells% in visceral fat and liver was higher in old mice than young PT mice (Fig.4a). We also carried out flow cytometry analysis using GFP and found similar results (Fig.4b), indicating that both tdTomato and GFP can be used to detect $p21^{high}$ cells using flow cytometry. While using BLI to detect $p21^{high}$ cells in dissected tissues from old mice, $p21^{high}$ cells were mainly found in visceral fat (Extended Data Fig.3), indicating the better sensitivity of fluorescence to detect $p21^{high}$ cells. In addition to aging, both DOXO treatment and HFD induced tdTomato+ $p21^{high}$ cells accumulation in visceral fat (Figs.4c and 4d) similarly to the findings using BLI (Figs.2b and 2c). Notably, *p21*-Cre is only activated (indicated by tdTomato) in a very small percentage (~0.1%) of DOXO-treated mouse embryonic fibroblasts (MEFs) with 2 copies of p21-Cre transgene, and the *p21*-Cre activity is higher in MEFs with 2 copies of transgene compared to 1 copy (Extended Data Fig.4). These findings indicate that the transgene is indeed working *in vitro*, and the low activity is likely due to low p21 promoter activity in cells *in vitro*. Altogether, these results suggest that $p21^{high}$ cells specifically accumulate in various tissues with aging or other conditions and can be precisely detected in our mouse models.

$p21^{high}$ cells exhibit features of cellular senescence.

In a previous study, we showed that $p21^{high}$ adipose-derived mesenchymal stem cells (ADSCs) accumulate in aged mice[41]. By single cell transcriptomics, these naturally occurring $p21^{high}$ cells appear to exhibit altered pathways commonly observed in senescent cells, including Senescent Cell Anti-Apoptotic Pathways (SCAPs; increased cell survival and decreased apoptosis) and NF-κB, IL6/JAK, mTOR, FOXO, and HMGB1 pathways[41]. Here, we further characterized $p21^{high}$ cells using our *p21*-Cre mouse model *in vivo*. We fed PL mice a HFD for 5 months to induce $p21^{high}$ cells in visceral fat (Fig.4d), isolated the stromal vascular fraction (SVF) from fat, and separated GFP+ $p21^{high}$ cells and GFP- non- $p21^{high}$ cells using fluorescence-activated cell sorting (FACS). Compared to GFP- cells, GFP+ $p21^{high}$ cells express 4-fold higher levels of *p21* as well as 6-fold and 4-fold higher

level of two major SASP components, *Il6* and *Cxcl1*. Notably, p16 mRNA levels are not statistically different between these 2 cell populations (Fig.5a). We also leveraged imaging flow cytometry (ImageStreamX) technology, which combines flow cytometry with high content image analysis, to further characterize these GFP+ *p21*^{high} cells at the single cell level. Enlarged size, senescence-associated-β-galactosidase (SA-β-gal), and proliferation arrest are 3 major features of senescent cells both *in vitro* and *in vivo*[30]. By analyzing the bright field (BF) images, GFP+ cells exhibit a larger cell size compared to GFP- cells (Fig.5b). We next stained SVF with SA-β-gal staining buffer and quantified SA-β-gal+ cells using a newly published method[42]. More than 60% of GFP+ cells were SA-β-gal+ compared to 40% in GFP- cells (Fig.5c). We also injected a thymidine analog, 5-ethyl-2′-deoxyuridine (EdU), into the mice, and assessed the incorporation of EdU using imaging flow cytometry 20 hours later. GFP- cells had more EdU+ cells (6%) than GFP+ cells (2%; Fig.5d), suggesting GFP+ cells had reduced proliferation rates. Loss of Lamin B1 is another commonly used marker for senescent cells[43]. By flow cytometry analysis, we found most GFP- cells (97%) expressed Lamin B1, while Lamin B1 was absent in 43% of GFP+ cells (Fig.5e). Altogether, *p21*^{high} cells exhibited several characteristics typical of senescent cells, including higher expression of *p21*, the SASP, enlarged size, SA-β-gal-positivity, reduced proliferation, loss of Lamin B1, and a number of altered senescence-associated pathways.

Inducible elimination of *p21*^{high} cells.

To enable elimination of *p21*^{high} cells in a temporal manner *in vivo*, we crossed PL mice with floxed diphtheria toxin A (DTA) mice[44], which contain a floxed-STOP cassette followed by DTA driven by the *ROSA* promoter (Fig.6a). We generated *p21*-Cre/+; LUC/DTA (PLD) mice (Fig.6a), which contain one copy of *p21*-Cre at the *Hipp11* locus, one copy of LUC at the *ROSA* locus, and one copy of DTA at the *ROSA* locus. Diphtheria toxin has two subunits, A and B. Subunit B is responsible for binding the receptor and internalization of DTA. Once inside cells, DTA inhibits eukaryotic translation elongation factor 2 (eEF2), leading to protein translation block and ensuing apoptosis[45]. Since PLD mice have only DTA without subunit B, it is theoretically unlikely that DTA leakage from *p21*^{high} cells (if any) could enter nearby non-*p21*^{high} cells and kill them. Thus, the PLD mice allow us to specifically kill (by DTA) as well as monitor *p21*^{high} cells (by LUC) *in vivo*. To validate clearance, we fed both PL and PLD mice a HFD for 4 months. After 2 doses of tamoxifen treatment, HFD-fed PL mice had high BLI signals, while the BLI signals were much lower in PLD mice (Fig.6b), demonstrating successful clearance of *p21*^{high} cells from obese mice. Two doses of tamoxifen treatment also reduced BLI signal in 23-month-old PLD mice compared to PL mice (Fig.6c), suggesting that *p21*^{high} cells can be eliminated using our model with aging as well.

Genetic inhibition of the SASP in *p21*^{high} cells *in vivo*.

The role of senescent cells has been extensively examined across a range of pathological conditions, while the underlying mechanisms have rarely been investigated *in vivo*. The SASP has long been speculated as one of the major mechanisms responsible for the harmful effects of senescent cells[2]. Here, we leveraged our *p21*-Cre mouse model to suppress the SASP exclusively in *p21*^{high} cells. The *NF-κB* pathway serves as a master regulator of the SASP[46], and *Rela* (v-rel reticuloendotheliosis viral oncogene homolog A, or *p65*) is

a crucial subunit for *NF-κB* activation[47]. Both *Rela* and the *NF-κB* pathway are highly activated in *p21*^{high} preadipocytes isolated from aged mice[41]. To inactivate the *NF-κB* pathway in *p21*^{high} cells, we crossed *p21*-Cre mice with floxed *Rela* mice[48], in which exon 1 of the *Rela* gene is flanked by loxP sites (Fig.7a). We generated *p21*Cre/+; Rela$^{fl/fl}$ (P-Rela) mice, which contain one copy of *p21*-Cre and two copies of floxed *Rela* and +/+; Rela$^{fl/fl}$ (Rela) mice, which only have two copies of floxed *Rela* (Fig.7b). We fed these mice a HFD for 3 months to induce *p21*^{high} cells. SVF cells were collected from visceral fat after 2 doses of tamoxifen administration to allow *Rela* mutation detection. We designed primers that generated a 164bp *Rela* mutant band and a 160bp WT band. *Rela* mutant bands were detected only in P-Rela SVF cells, while WT bands were detected in both P-Rela and Rela SVF cells (Fig.7c). The *Rela* mutation was further confirmed by sequencing the *Rela* mutant bands. In addition, *Rela* mutant bands were much fainter than WT bands, and strong WT bands were also observed in P-Rela SVF cells, indicating that only a small percent of P-Rela SVF cells (*p21*^{high} cells) had the *Rela* mutation. We next interrogated whether the *Rela* mutation lead to SASP inhibition. We crossed CAG-Cre mice[49], which carry a constitutively active CAG promoter driving Cre, with floxed Rela mice to generate CAG-Cre/+; Rela$^{fl/fl}$ (CAG-Rela) mice. We isolated ear fibroblasts from these mice and induced senescence using DOXO. After 4-OHT treatment to induce Cre, expression levels of *Rela* and several key SASP components were reduced by 40-70% in senescent CAG-Rela cells compared to senescent WT cells (Fig.7d). Thus, the SASP of senescent cells can be genetically suppressed in our models.

Clearance of *p21*^{high} cells improves physical function.

Physical function declines with aging, leading to physical frailty, compromised systemic homeostasis, and increased vulnerability to stresses[50]. We next investigated whether *p21*^{high} cells play a causal role in physical frailty with aging. We treated 20-month-old PL and PLD mice with 2 doses of tamoxifen per month for 3 months (Fig.8a) to eliminate *p21*^{high} cells in PLD mice (Fig.6c). We assessed physical frailty following the frailty criteria widely used in clinic practice[51,52], including weight loss, walking speed, grip strength, physical endurance, food intake, and daily activity. No difference was observed in body weight, maximal walking speed, or grip strength between 20-month-old PL and PLD mice before tamoxifen treatment. After 3 months of intermittent tamoxifen administration (total 6 doses), maximal walking speed, grip strength, hanging endurance, daily food intake, and daily activity were all significantly higher in PLD mice than PL mice, while body weight changes were not statistically different (Fig.8b–g). These results demonstrate that clearance of *p21*^{high} cells alleviate physical frailty in old mice.

Discussion

In this technical report, we present a mouse model that enables us to investigate the role and underlying mechanisms of *p21*^{high} cells in various conditions, including obesity and aging. Senescent cells are highly heterogeneous, and no single marker has been shown to be sufficient to define senescent cells[31]. Up to now, to our knowledge, most mouse models in the field[15,16,26,27] were designed to exclusively target *p16*^{high} cells, limiting our perspective on senescence biology. Here, we characterized a previously unexplored

senescent cell population, *p21*^{high} cells. We found that *p21*^{high} cells accumulate in tissues with aging and obesity, and that these cells exhibit a number of typical features of senescent cells. Moreover, single cell transcriptomic analysis reveals that *p21*^{high} cells and *p16*^{high} cells are two distinct cell populations in a number of aged tissues, suggesting that the role of *p21*^{high} cells in various age-related conditions could be different from *p16*^{high} cells. Thus, future investigations using this model focusing on *p21*^{high} cells could provide key novel insights into the biology of aging, pathogenesis of chronic diseases of aging and the discovery of novel geroscience-guided interventions.

Both *p21* and *p16* are cell cycle regulators and are widely expressed across a range of cells and tissues at relatively low levels. It is possible that models leveraging these two markers for senescent cells might target some non-senescent cells, especially in the models using a knock-in strategy. Since senescent cells accumulate exponentially in aged mice (older than 20-month-old)[53–55], it is critically important to precisely identify the cells targeted by these models in aged tissues, not just in young to middle-aged tissues. The *p21*-Cre mouse model presented here was made by introducing a transgene containing the *p21* promoter driving Cre, which is likely to have a high threshold for Cre activation. Using PT mice, we found that percentages of *p21*^{high} cells varied from 1.5 to 10% across a number of tissues in 23-month-old mice, which is consistent with the percent of senescent cells in aged mice[42], while few tdTomato+ *p21*^{high} cells (<1%) were observed in young tissues. Moreover, *p21*^{high} cells targeted by this model showed typical features of senescent cells (Fig.5). Therefore, our *p21*-Cre mouse model seems to only target a small number of cells, which only accumulate with aging or other pathological conditions. Importantly, intermittent clearance of these cells was sufficient to improve age-associated physical dysfunction (Fig.8), consistent with findings using senolytic drugs[13].

The *p21*-Cre mouse model offers various opportunities to study *p21*^{high} cells *in vivo*. As demonstrated in this report, we can monitor, sort, image, eliminate, or modulate *p21*^{high} cells by crossing this model with different floxed mice. Inducible Cre allows us to intermittently clear *p21*^{high} cells in later life, in contrast to continuous clearance, and is more clinically relevant. Notably, our strategy of eliminating *p21*^{high} cells is distinct from interference with *p21* gene function. As a cyclin-dependent kinase inhibitor, *p21* plays an essential role in a wide range of cellular events. Inactivation or suppression of the *p21* gene *in vivo* is likely to have severe side effects, such as tumorigenesis[56]. Our strategy here is to leverage *p21* as a marker to eliminate *p21*^{high} cells. In addition, the *p21*-Cre transgene was specifically inserted into *H11* locus, rather than the native *p21* locus. Theoretically, this is less likely to affect function and regulation of the *p21* gene. PL mice also offer a unique opportunity for us to assess *p21*^{high} senescent cell burden in live mice. PL mice are distinct from *p21*[38,57] or *p16*[16,54] reporter mice, which are currently used for monitoring the load of senescent cells *in vivo*[19,25,58]. The expression of LUC from all these reporter mice is driven by either the *p16* or *p21* promoter. Since *p16* and *p21* expression levels may fluctuate and are highly variable across different cell types, the BLI signals observed in these reporter mice likely indicate the *p16* or *p21* promoter activity *in vivo*, rather than the absolute numbers of *p16*^{high} or *p21*^{high} cells. Our PL mouse model is mechanistically distinct. After a STOP fragment is excised by Cre in *p21*^{high} cells in PL mice, expression of LUC in these cells is driven by *Gt(ROSA)26Sor* promoter, which is ubiquitously and stably active in most prenatal and

postnatal cells and tissues[59]. Therefore, compared to *p21* or *p16* reporter mice, the BLI signals in PL mice more likely represent the number of $p21^{high}$ cells *in vivo*. This makes PL mice more suited for screening drugs that can kill $p21^{high}$ cells, because a reduction in BLI signals in PL mice indicates clearance of $p21^{high}$ cells, rather than inhibition of *p21* promoter activity. This is important since drugs that reduce *p21* promoter activity (thus interfere *p21* gene function as a tumor suppressor) will likely initiate tumorigenesis[56]. Thus, these mice can be indispensable models for screening novel senolytic drugs to kill $p21^{high}$ cells *in vivo* and greatly accelerate next-generation senolytic drug development and senescence biomarker discovery.

The underlying mechanisms of how senescent cells cause tissue dysfunction are largely unknown *in vivo*. The SASP has been considered to be one major mechanism and a number of SASP inhibitors can improve healthspan in aged mice, including JAK inhibitors[8,9,60], metformin[61,62], and rapamycin[63–65]. However, it is difficult to distinguish effects of these inhibitors on senescent cells from other cells. The *p21*-Cre mouse model allows us to suppress the SASP only in $p21^{high}$ cells, thus is a cleaner system for examining the contribution of the SASP to age-related disorders. Moreover, using this tool, we can modulate specific SASP components or multiple genes of interest (any gene located outside chromosome 11, since the *p21*-Cre is located on chromosome 11) specifically in $p21^{high}$ cells, which will be valuable for the senescence field.

In summary, our study demonstrates that the *p21*-Cre mouse model is a valuable and powerful model for studying $p21^{high}$ cells and could initiate a new avenue of research to further understand the biology of senescent cells.

Methods

p21-Cre mouse model generation.

A 7 kb DNA fragment was synthesized by GenScript (Piscataway, NJ), containing a 3225 bp mouse p21 promoter fragment followed by a bicistronic message consisting of the coding sequence for Cre fused to a tamoxifen-inducible estrogen receptor (ER^{T2}) domain. An internal ribosome entry site (IRES) followed by an open reading frame (ORF) coding for enhanced green fluorescent protein (EGFP) was also added into the transgene. The synthesized fragment (*p21*-ER-Cre) was subcloned into vector pBT378 for generating *p21*-Cre mice through Integrase-mediated transgenesis (IMT). Briefly, the *p21*-ER-Cre-pBT378 construct was microinjected into the pronucleus of recipient zygotes containing attP sites in the Hipp11 locus, which has a high recombination rate and results in stable expression of a single copy of the transgene (done at the Transgenic Research Center in Stanford University). Site-specific recombination occurred between the attB sites in the plasmid and attP sites in the H11 genomic locus. Positive embryonic stem (ES) cell clones were then implanted into C57BL/6 females. A positive founder mouse was confirmed by PCR using a set of primers flanking the recombined 5'- and 3'- attP/attB sites in the H11 locus, as well as sets of specific primers that amplify unique sequences within the transgene. The investigators are happy to share the *p21*-Cre mouse model with the research community. Please contact Dr. Ming Xu at mixu@uchc.edu to request the mouse model. The mice will

be shipped after a Material Transfer Agreement (MTA) is approved by Mayo Clinic. For non-profit research purpose, the requestor will be only responsible for the shipping cost.

Mouse models and drug treatments.

All animal experiments were performed according to protocols approved by the Institutional Animal Care and Use Committee (IACUC) at UConn Health. All mice were maintained in a pathogen-free facility at 23–24 °C with humidity of 30-60% under a 12-h light, 12-h dark regimen with free access to a RCD (Teklad global 18% protein, Envigo #2918, Indianapolis, IN), or a 60% (by calories) HFD (D12492, irradiated; Research Diets, New Brunswick, NJ) and water. For tamoxifen treatment, tamoxifen (Sigma-Aldrich, St Louis, MO) was dissolved in corn oil, and was administrated to mice by intraperitoneal (i.p.) injection one dose (2 mg per mouse) daily for two consecutive days. For DOXO treatment, DOXO (Sigma-Aldrich) was given to mice (20 mg/kg) once by i.p. injection. Tamoxifen was given one dose at the same time of DOXO administration, and one more dose was given 16 h after. Floxed tdTomato mice (#007914), floxed LUC mice (#005125), floxed DTA mice (#009669), CAG-Cre mice (#004682), and $Rela^{fl/fl}$ mice (#024342) were all purchased from the Jackson Laboratory.

Single cell RNA-seq analysis.

Single cell RNA-seq data was collected from the *Tabula Muris Senis* single cell transcriptomic atlas for aged mice[32]. Data were visualized using the provided browser based platform available at https://tabula-muris-senis.ds.czbiohub.org/. In brief, single cell RNA seq data was examined from visceral adipose tissue (FACS method), liver (droplet method), and heart (droplet method). To account for differences in animal ages available for each tissue, all available data from animals 18 months or older was included in our analysis (Fat: 18 and 24 months; Liver: 18, 21, 24, 30 months; Heart: 18, 21, 24, 30 months). Expression profiles were then captured for *p21* and *p16* in each tissue.

Tissue dissociation.

Visceral fat and liver tissues were minced with scissors, and digested in PBS containing 1 mg/ml type II collagenase (Sigma-Aldrich) and 10 μg/ml DNase I (Sigma-Aldrich) at 37°C for 1 h. After digestion, stromal vascular fraction (SVF) cells were separated from visceral fat. SVF cells and liver cells were washed with PBS/2% FBS and filtered through 100 μm cell strainer. Cells were then incubated with ACK lysing buffer (Thermo Fisher Scientific, Waltham, MA) at room temperature for 10 min to remove red blood cells. Cells were washed with PBS/2% FBS for further experiments.

SA-β-gal staining.

SA-β-gal staining was assayed as previously described[9,42]. Briefly, purified SVF cells were fixed in 4% paraformaldehyde (PFA, Thermo Fisher Scientific) for 15 min at room temperature. Cells were washed with PBS, then incubated with SA-β-gal staining solution containing 1 mg/ml X-gal (Teknova, Hollister, CA), 40 mM citric acid/sodium phosphate at pH 6.0, 5 mM potassium ferrocyanide, 5 mM potassium ferricyanide, 150 mM NaCl, and 2 mM $MgCl_2$ at 37 °C in a humidified chamber, and protected from light. After

16 h incubation, cells were washed in ice-cold PBS to stop the enzymatic reaction and resuspended in PBS buffer for ImageStreamX analysis.

EdU staining.

Mice fed HFD for 5 months were treated with 1 mg/kg 5-ethynyl-2′-deoxyuridine (EdU, Cayman Chemical, Ann Arbor, MI) via intraperitoneal injection. After 20 h, SVF cells were isolated and fixed in 4% PFA for 15 min at room temperature. After being washed with PBS/1% BSA, cells were permeabilized by 0.3% Triton X-100, and stained with 100 mM Tris-HCl (pH 7.5), 2 mM $CuSO_4$, 10 mM ascorbic acid, 2 μM Alexa Fluor 647 azide (Thermo Fisher Scientific) for 30 min at room temperature. Cells were washed with PBS/1% BSA twice, incubated with 0.1 μg/ml DAPI (Sigma-Aldrich) for 5 min, and analyzed by ImageStreamX.

Imaging flow cytometry analysis.

SVF cells stained with SA-β-gal, EdU, or p21 antibody were imaged by ImageStreamX Mark II (Amnis, Seattle, WA) and analyzed by IDEAS 6.2 software (Amnis). To focus cells, samples were gated using gradient RMS values of brightfield channel. Cells were further gated using brightfield area and aspect ratio to select single cells. GFP- and GFP+ SVF cells were measured for cell areas using brightfield area. Mean pixel of brightfield was used to calculate SA-β-gal intensity in GFP- and GFP+ SVF cells as previously described[42]. Low passage wildtype mouse ear fibroblasts stained with SA-β-gal were used as control. Notably, SA-β-gal staining did not significantly affect the GFP signal in SVF cells from obese PL mice. To measure EdU, the intensity of Alexa Fluor 647 channel was compared between GFP- and GFP+ SVF cells. Wildtype young mice SVF cells with staining buffer but without EdU injection were used as control. tdTomato− and tdTomato+ SVF cells were measured for *p21* expression using the intensity of Alexa Fluor 647 channel. The SVF cells from same old PT mice but without anti-*p21* primary antibody were used as control for p21 expression.

Cell culture.

Mouse embryonic fibroblasts (MEFs) were isolated from embryos between embryonic day 13.5-14.5 of gestation with their head, tail, limbs and visceral organs removed. The embryo carcass was washed with PBS, minced thoroughly with scissors before being dissociated in 0.05% trypsin-EDTA (Thermo Fisher Scientific) at 37°C for 15 min. Then embryo tissue was pipetted up and down, and filtered through cell strainer. Single cells were seeded into culture plates in DMEM high glucose (Thermo Fisher Scientific) containing 10% fetal bovine serum (FBS, Corning, Corning, NY) and 1% penicillin-streptomycin (Thermo Fisher Scientific). Cells were cultured at 37°C in a humidified 5% CO_2 and 3% O_2 incubator. To test the *p21-Cre* activity *in vitro*, MEFs were treated with 0.5 μM DOXO for 24 h and 0.5 μM 4-OHT (Sigma-Aldrich) for 3 days. Ear fibroblasts were isolated as described previously[66]. To induce senescence, ear fibroblasts were treated with 0.5 μM DOXO for 24 h, and considered to be senescent 10 days after.

Immunofluorescence staining.

SVF cells were fixed in 4% PFA for 15 min at room temperature. Cells were then washed with PBS prior to a 10 min incubation in permeabilization buffer (0.2% Triton X-100, 1% BSA in PBS). Next, the cells were washed with PBS and blocked for 1 h in PBS/1% BSA solution. After blocking, cells were incubated with anti-Lamin B1 primary antibody (1:100, 12987-1-AP, Proteintech, Rosemont, IL) or anti-p21 primary antibody (1:40, 14-6715-81, Thermo Fisher Scientific) in PBS/1% BSA overnight at 4 °C. The next day, cells were washed with PBS and incubated for 1 h at room temperature with Alexa Fluor 647-conjugated anti-rabbit secondary antibody (A-21244, Thermo Fisher Scientific) diluted 1:200 in PBS/1% BSA. Stained cells were then washed with PBS and analyzed by flow cytometry or ImageStreamX.

Flow cytometry analysis.

SVF cells and liver cells were isolated from visceral fat and liver tissues, and washed with PBS/2% FBS. Cells were stained with 0.1 μg/ml of DAPI for 5 min and detected by BD LSR II flow cytometer (BD Biosciences, San Jose, CA). Data analysis was performed on the FlowJo V10.7 software. SVF cells and liver cells from wildtype young mice were used as control for tdTomato and GFP expression. For Lamin B1 expression, the SVF cells from same obese PL mice but without anti-Lamin B1 primary antibody were used as control.

Fluorescence-activated cell sorting (FACS).

SVF cells were isolated from mice fed HFD for 5 months, cells were sorted into GFP- and GFP+ populations through BD FACSAria II flow cytometer (BD Biosciences). Sorted cells were used to detect *p21*, *p16* and SASP expression.

Bioluminescence imaging.

Mice were anesthetized with isoflurane (Piramal Critical Care, Bethlehem, PA) gas and injected intraperitoneally with 3 mg D-luciferin (Gold Biotechnology, St. Louis, MO) in 200 μl PBS. 5 min after injection, mice were placed in IVIS spectrum in vivo imaging system (PerkinElmer, Waltham, MA) and bioluminescence images were subsequently captured with 3 min exposure time. Region of interest (ROI) was manually selected in a consistent way for individual mouse in same cohort. Bioluminescent signal of ROI was calculated using the Living Image 4.5.5 software (PerkinElmer). Bioluminescence images of brain, lung, heart, pancreas, spleen, kidney, liver, intestine, inguinal fat, visceral fat, and muscle tissues were also captured from young and old PL mice.

Histological analysis.

Visceral fat, liver, intestine, brain, heart, muscle tissues were fixed with 4% PFA overnight at 4°C. After being washed with PBS, tissues were then transferred to 30% sucrose (Sigma-Aldrich) overnight at 4°C, and embedded in OCT compound (Thermo Fisher Scientific). Liver, intestine, brain, heart, muscle tissues in OCT blocks were cut into 6 μm thickness sections on Leica CM3050 S cryostat, and visceral fat tissues were cut into 10 μm thickness sections. Nuclei were counterstained with Hoechst 33342 (Thermo Fisher Scientific) and imaged on a fluorescence microscope (Zeiss, Jena, Germany). To quantify tdTomato+ cells,

three sections from each mouse were scanned and then counted using ImageJ (v1.51g) software.

Physical function measurements.

Physical function measurements were performed as previously described[13]. To test muscle strength and neuromuscular function, maximal walking speed, grip strength and grid hanging test were performed in aged mice. Maximal walking speed was tested by accelerating 4 lane RotaRod system (Columbus Instruments, Columbus, OH). Mice were trained on the RotaRod for consecutive 2 d at a constant speed of 4 r.p.m. for 300 s. The day after the last day of training, mice were acclimatized to the testing room for 30 min. RotaRod test was started at 4 r.p.m. and accelerated from 4 to 47.2 r.p.m. in 6 min. The speed was recorded when the mouse fell off, the average of 4 trials were calculated and normalized to the baseline speed. Forelimb grip strength (g) was assessed by a grip strength test meter (Bioseb, France). Results were averaged over 10 trials. Grid hanging test was performed on the grid which was placed onto a holding apparatus at a 35 cm distance from the floor, a soft pad was used to avoid injuries. Hanging time was recorded when the mouse fell off, the average of 3 trials were calculated and normalized to body weight as hanging duration (sec) × body weight (g). A threshold at 7 min was set to consider the maximum hanging time.

Comprehensive laboratory animal monitoring system (CLAMS).

Daily activity, food and water intake, metabolic performance, temperature were measured for the 23 months old PL and PLD mice on a CLAMS system equipped with Oxymax open-circuit calorimeter (Columbus Instruments, Columbus, OH). Physiological and behavioral parameters for individual mouse were monitored over a 24 h period (12 h light/dark cycle), and results were analyzed by CLAX software (Columbus Instruments).

DNA preparation and PCR.

Rela and P-Rela mice were sacrificed 24 h after tamoxifen injection for 3 doses. Genomic DNA was extracted by lysing the SVF cells in an alkaline reagent containing 25 mM NaOH and 0.2 mM EDTA at 94°C for 2 h and neutralizing with equal volume of 40 mM Tris-HCl (pH 7.4), followed by purifying with isopropanol and 75% ice-cold ethanol (Sigma-Aldrich). Equal amount of DNA for each sample was adopted to react with GoTaq Green Master Mix (Promega, Madison, WI) and indicated genotyping primers, respectively. PCR products were separated on a 2% agarose gel with SYBR safe DNA gel stain (Thermo Fisher Scientific) running in TAE buffer (Bio-Rad, Hercules, CA) and visualized by ChemiDoc MP imaging system (Bio-Rad). All primers were purchased from Integrated DNA Technologies (IDT, Coralville, IA). Primer sequences (5′ to 3′) are listed below.

Cre-F: ACCAGCCAGCTATCAACTCG;

Cre-R: TACATTGGTCCAGCCACC;

SH176-F: TGGAGGAGGACAAACTGGTCAC;

SH178-R: TTGTTCCCTTTCTGCTTCATCTTGC;

BT436-R: ATCAACTACCGCCACCTCGAC;

Rela-F: GACACGCTGAACTTGTGGCCGTTTA;

Rela-WT-R: TATCATGTCTGGATCAATTCATAAC;

Rela-Cut-R: TTTCGACCTGCAGCCAATAAGCT

RNA extraction and real-time PCR.

Cells were collected, lysed in TRIzol reagent (Thermo Fisher Scientific) and then extracted with chloroform, isopropanol and 75% ice cold ethanol (Sigma-Aldrich). RNA was dissolved in RNase free water, and reverse transcribed to cDNA with M-MLV reverse transcriptase kit (Thermo Fisher Scientific). Quantitative real-time PCR was conducted in four or five duplicates using PerfeCTa FastMix II (Quantabio, Beverly, MA) on CFX96 Real-Time PCR detection system (Bio-Rad). The relative mRNA level of target genes was normalized to TATA-binding protein (*Tbp*) and calculated via the $2^{-\Delta\Delta CT}$ method. Probes and primers for *Tbp*, *p21*, *p16*, *Il6*, *Cxcl1*, *Ccl2* and *Rela* were purchased from Integrated DNA Technologies (IDT, Coralville, IA).

Statistics and Reproducibility

Sample sizes were determined using power analysis based on the means and variation of pilot experiments and previous publications[9,13]. No data was excluded. Mice were assigned to experimental groups based on their genotypes. Investigators were blinded to allocation during experiments and outcome assessments. Data was analyzed using Prism 7 (Graphpad Inc.).

Data Availability Statement

The source data are published with the manuscript and are available from the corresponding author upon reasonable request. The link for Tabula Muris Senis database is https://tabula-muris-senis.ds.czbiohub.org/.

Extended Data

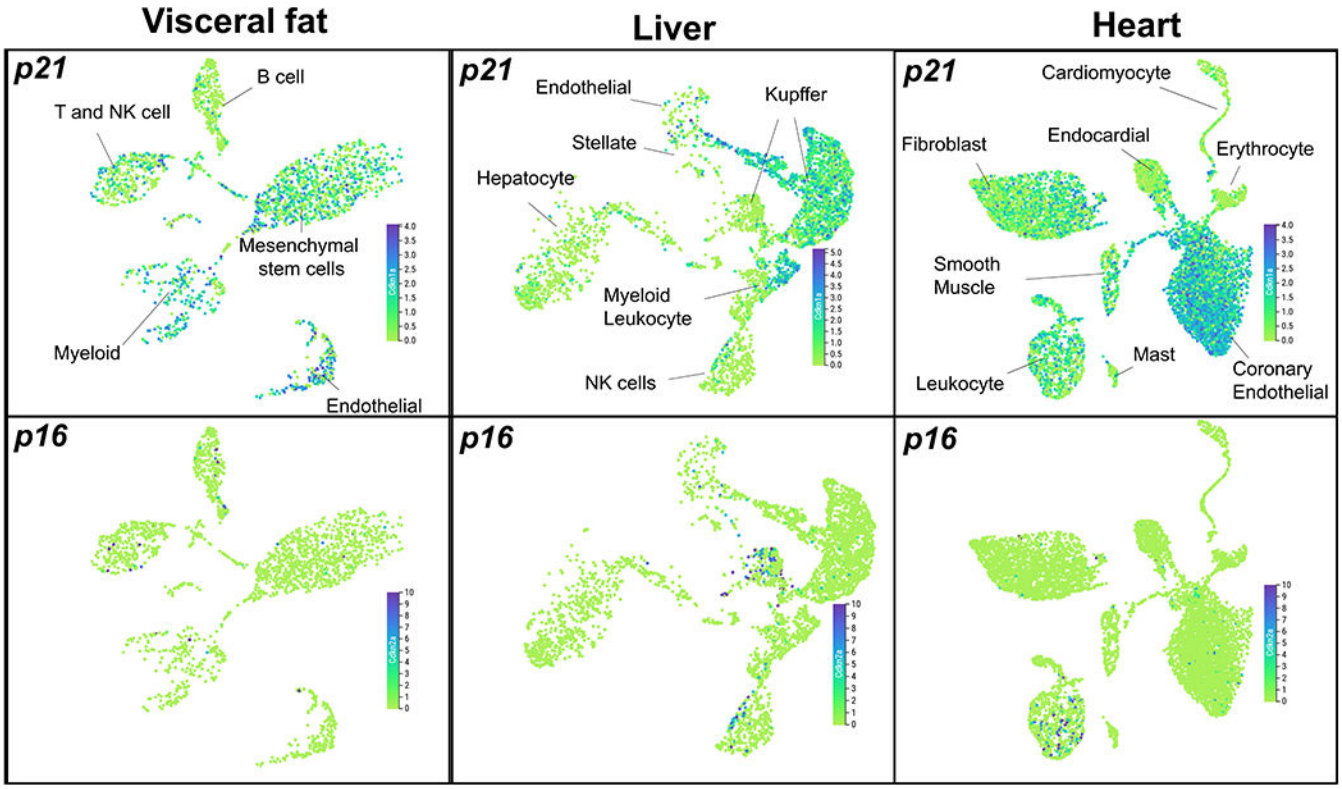

Extended Data Fig. 1. *p16*^{high} and *p21*^{high} cells are two distinct cell populations in aged tissues.

Uniform manifold approximation and projection (UMAP) plots showing expression levels of *p21* (*cdkn1a*) and *p16* (*cdkn2a*) in visceral fat, liver and heart in 18-30 months old mice. The figures were generated using the *Tabula Muris Senis* interactive platform (https://tabula-muris-senis.ds.czbiohub.org/).

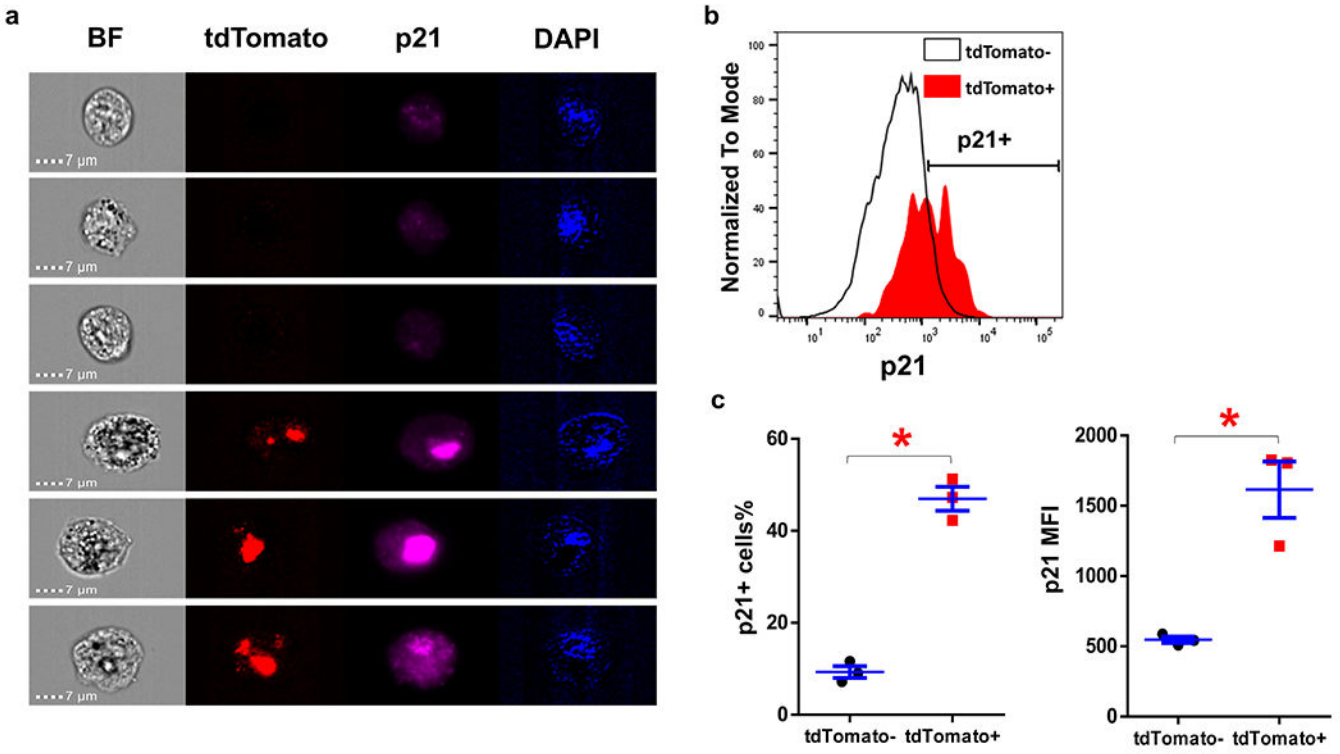

Extended Data Fig. 2. *p21* expression in tdTomato+ and tdTomato− cells in old mice.
(a) Representative images of tdTomato+ and tdTomato− SVF cells in old PT mice. **(b)** *p21* staining intensity of tdTomato+ and tdTomato− SVF cells detected by flow cytometry. **(c)** *p21*+ cells percentage and *p21* mean fluorescence intensity (MFI) of tdTomato+ and tdTomato− SVF cells. For c, n=3 for both groups. Results were shown as mean ± s.e.m. * $p<0.05$; two-tailed, paired Student's t-test. $p=0.009$ for *p21*+ cells%; $p=0.028$ for *p21* MFI.

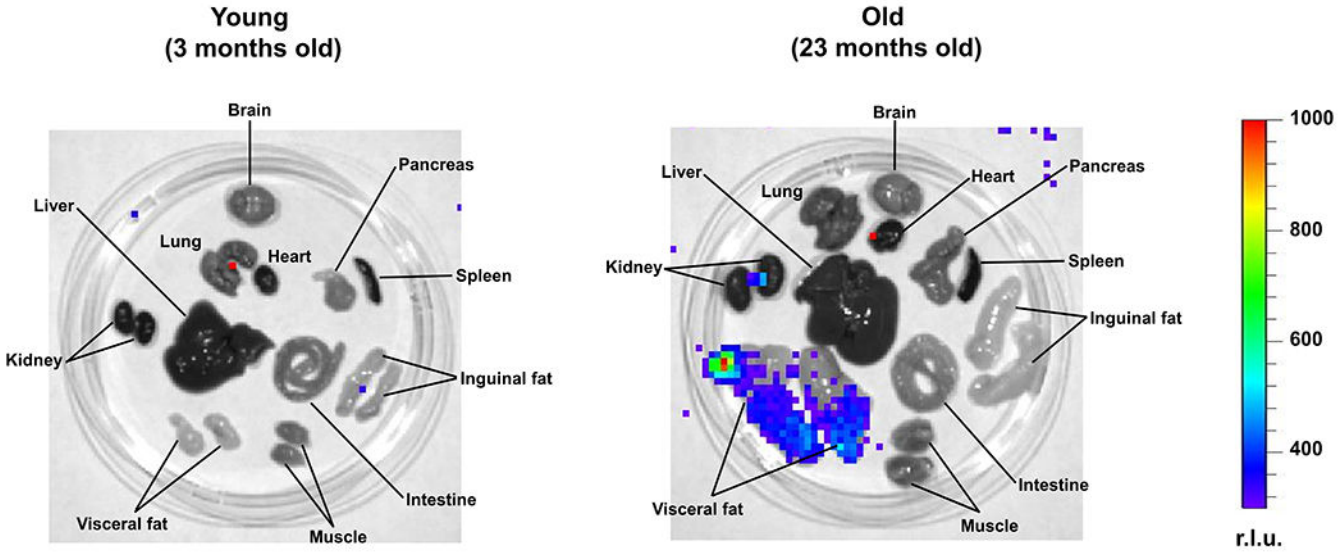

Extended Data Fig. 3. Tissue distribution of *p21*^{high} cells.

Representative images of LUC activity in various tissues from young and old mice. r.l.u., relative luciferase units.

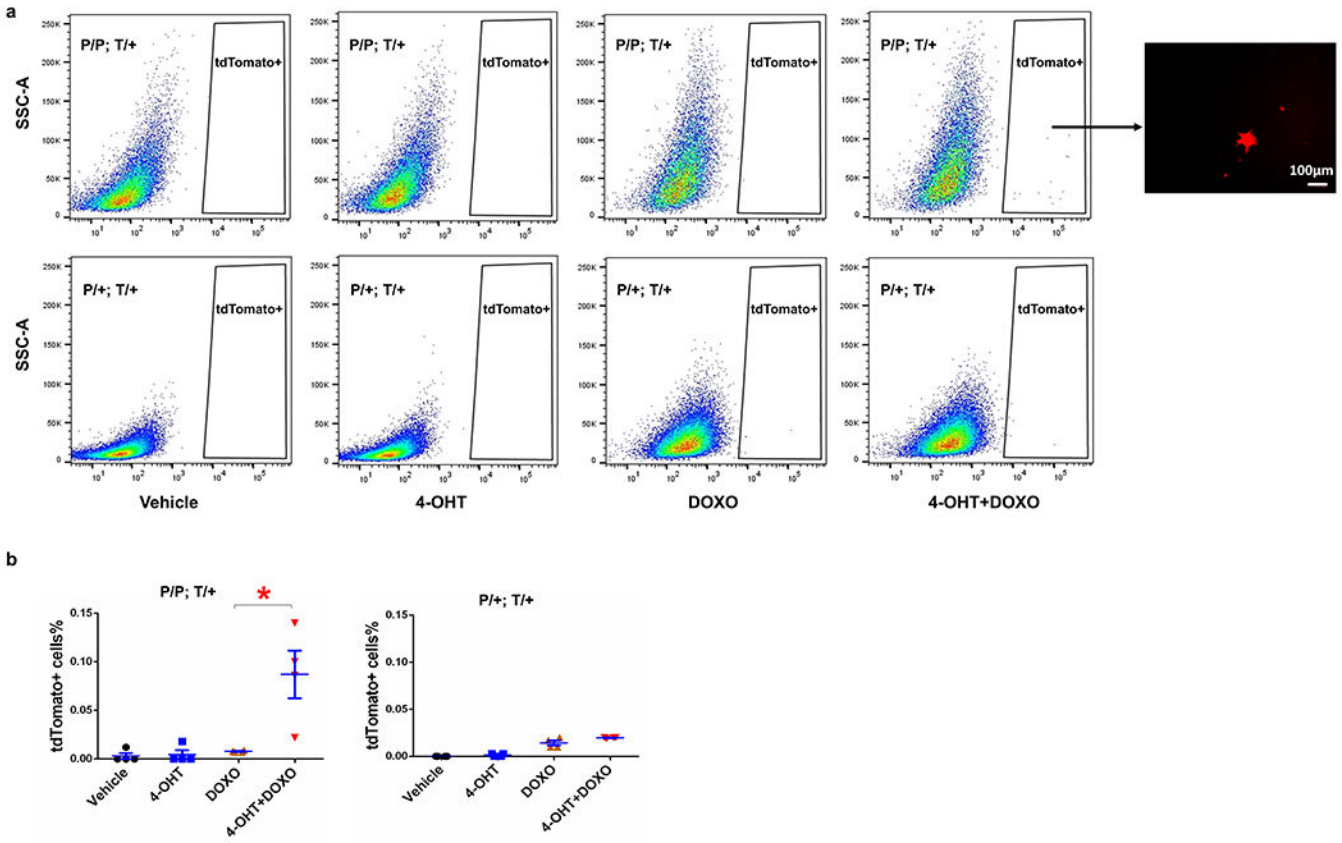

Extended Data Fig. 4. The activity of *p21-Cre* is low in cells *in vitro*.

(a) Flow cytometry analysis of tdTomato (T) in MEFs (P/P; T/+ and P/+; T/+). Representative image of tdTomato+ cells can be only seen in P/P; T/+ MEFs treated with both 4-OHT and DOXO. **(b)** tdTomato+ cells percentage in MEFs. For b, n=4 for all groups. Results were shown as mean ± s.e.m. * p= 0.018; two-tailed, unpaired Student's t-test.

Supplementary Material

Refer to Web version on PubMed Central for supplementary material.

Acknowledgements

The authors are grateful to colleagues in the UConn Center on Aging for helpful and constructive discussion, Zhifang Hao for histology service, and Stefanie Farkas for administrative assistance. This work was supported in part by the Regenerative Medicine Initiative for Diabetes-Career Development Award from Mayo Clinic (M.X.), Glenn Foundation for Medical Research and AFAR Grant for Junior Faculty (M.X.), Robert and Arlene Kogod (J.L.K.), the Connor Group (J.L.K.), Robert J. and Theresa W. Ryan (J.L.K.), the Noaber Foundation (J.L.K.), Travelers Chair in Geriatrics and Gerontology (G.A.K.), and NIH grants R37AG013925 (J.L.K.), P01AG062413 (J.L.K.), R33AG061456 (J.L.K., T.T., G.A.K.), AG063528 (M.X.), AG066679 (M.X.), and AG068860 (M.X.).

Reference

1. Gorgoulis V et al. Cellular Senescence: Defining a Path Forward. Cell 179, 813–827, doi:10.1016/j.cell.2019.10.005 (2019). [PubMed: 31675495]
2. Tchkonia T, Zhu Y, van Deursen J, Campisi J & Kirkland JL Cellular senescence and the senescent secretory phenotype: therapeutic opportunities. The Journal of clinical investigation 123, 966–972, doi:10.1172/JCI64098 (2013). [PubMed: 23454759]
3. Kirkland JL & Tchkonia T Cellular Senescence: A Translational Perspective. EBioMedicine 21, 21–28, doi:10.1016/j.ebiom.2017.04.013 (2017). [PubMed: 28416161]
4. Kuilman T et al. Oncogene-induced senescence relayed by an interleukin-dependent inflammatory network. Cell 133, 1019–1031, doi:10.1016/j.cell.2008.03.039 (2008). [PubMed: 18555778]
5. Wang C et al. DNA damage response and cellular senescence in tissues of aging mice. Aging Cell 8, 311–323, doi:10.1111/j.1474-9726.2009.00481.x (2009). [PubMed: 19627270]
6. Zhu Y, Armstrong JL, Tchkonia T & Kirkland JL Cellular senescence and the senescent secretory phenotype in age-related chronic diseases. Current opinion in clinical nutrition and metabolic care 17, 324–328, doi:10.1097/MCO.0000000000000065 (2014). [PubMed: 24848532]
7. Baker DJ et al. Naturally occurring p16(Ink4a)-positive cells shorten healthy lifespan. Nature 530, 184–189, doi:10.1038/nature16932 (2016). [PubMed: 26840489]
8. Xu M et al. Targeting senescent cells enhances adipogenesis and metabolic function in old age. Elife 4, e12997, doi:10.7554/eLife.12997 (2015). [PubMed: 26687007]
9. Xu M et al. JAK inhibition alleviates the cellular senescence-associated secretory phenotype and frailty in old age. Proceedings of the National Academy of Sciences of the United States of America 112, E6301–6310, doi:10.1073/pnas.1515386112 (2015). [PubMed: 26578790]
10. Kirkland JL, Tchkonia T, Zhu Y, Niedernhofer LJ & Robbins PD The Clinical Potential of Senolytic Drugs. Journal of the American Geriatrics Society 65, 2297–2301, doi:10.1111/jgs.14969 (2017). [PubMed: 28869295]
11. Acosta JC et al. A complex secretory program orchestrated by the inflammasome controls paracrine senescence. Nature cell biology 15, 978–990, doi:10.1038/ncb2784 (2013). [PubMed: 23770676]
12. Nelson G et al. A senescent cell bystander effect: senescence-induced senescence. Aging Cell 11, 345–349, doi:10.1111/j.1474-9726.2012.00795.x (2012). [PubMed: 22321662]
13. Xu M et al. Senolytics improve physical function and increase lifespan in old age. Nature medicine 24, 1246–1256, doi:10.1038/s41591-018-0092-9 (2018).
14. da Silva PFL et al. The bystander effect contributes to the accumulation of senescent cells in vivo. Aging Cell 18, e12848, doi:10.1111/acel.12848 (2019). [PubMed: 30462359]
15. Baker DJ et al. Clearance of p16Ink4a-positive senescent cells delays ageing-associated disorders. Nature 479, 232–236, doi:10.1038/nature10600 (2011). [PubMed: 22048312]
16. Demaria M et al. An essential role for senescent cells in optimal wound healing through secretion of PDGF-AA. Developmental cell 31, 722–733, doi:10.1016/j.devcel.2014.11.012 (2014). [PubMed: 25499914]
17. Farr JN et al. Targeting cellular senescence prevents age-related bone loss in mice. Nature medicine 23, 1072–1079, doi:10.1038/nm.4385 (2017).
18. Palmer AK et al. Targeting senescent cells alleviates obesity-induced metabolic dysfunction. Aging Cell, e12950, doi:10.1111/acel.12950 (2019). [PubMed: 30907060]
19. Jeon OH et al. Local clearance of senescent cells attenuates the development of post-traumatic osteoarthritis and creates a pro-regenerative environment. Nature medicine 23, 775–781, doi:10.1038/nm.4324 (2017).
20. Bussian TJ et al. Clearance of senescent glial cells prevents tau-dependent pathology and cognitive decline. Nature 562, 578–582, doi:10.1038/s41586-018-0543-y (2018). [PubMed: 30232451]
21. Roos CM et al. Chronic senolytic treatment alleviates established vasomotor dysfunction in aged or atherosclerotic mice. Aging Cell 15, 973–977, doi:10.1111/acel.12458 (2016). [PubMed: 26864908]

22. Childs BG et al. Senescent intimal foam cells are deleterious at all stages of atherosclerosis. Science 354, 472–477, doi:10.1126/science.aaf6659 (2016). [PubMed: 27789842]
23. Ogrodnik M et al. Cellular senescence drives age-dependent hepatic steatosis. Nature communications 8, 15691, doi:10.1038/ncomms15691 (2017).
24. Schafer MJ et al. Cellular senescence mediates fibrotic pulmonary disease. Nature communications 8, 14532, doi:10.1038/ncomms14532 (2017).
25. Chang J et al. Clearance of senescent cells by ABT263 rejuvenates aged hematopoietic stem cells in mice. Nature medicine 22, 78–83, doi:10.1038/nm.4010 (2016).
26. Grosse L et al. Defined p16(High) Senescent Cell Types Are Indispensable for Mouse Healthspan. Cell Metab 32, 87–99 e86, doi:10.1016/j.cmet.2020.05.002 (2020). [PubMed: 32485135]
27. Omori S et al. Generation of a p16 Reporter Mouse and Its Use to Characterize and Target p16(high) Cells In Vivo. Cell Metab 32, 814–828 e816, doi:10.1016/j.cmet.2020.09.006 (2020). [PubMed: 32949498]
28. Hall BM et al. p16(Ink4a) and senescence-associated beta-galactosidase can be induced in macrophages as part of a reversible response to physiological stimuli. Aging (Albany NY) 9, 1867–1884, doi:10.18632/aging.101268 (2017). [PubMed: 28768895]
29. Frescas D et al. Murine mesenchymal cells that express elevated levels of the CDK inhibitor p16(Ink4a) in vivo are not necessarily senescent. Cell Cycle 16, 1526–1533, doi:10.1080/15384101.2017.1339850 (2017). [PubMed: 28650766]
30. Di Micco R, Krizhanovsky V, Baker D & d'Adda di Fagagna F Cellular senescence in ageing: from mechanisms to therapeutic opportunities. Nat Rev Mol Cell Biol, doi:10.1038/s41580-020-00314-w (2020).
31. Roy AL et al. A Blueprint for Characterizing Senescence. Cell 183, 1143–1146, doi:10.1016/j.cell.2020.10.032 (2020). [PubMed: 33128870]
32. Tabula Muris C A single-cell transcriptomic atlas characterizes ageing tissues in the mouse. Nature 583, 590–595, doi:10.1038/s41586-020-2496-1 (2020). [PubMed: 32669714]
33. Feil R, Wagner J, Metzger D & Chambon P Regulation of Cre recombinase activity by mutated estrogen receptor ligand-binding domains. Biochem Biophys Res Commun 237, 752–757 (1997). [PubMed: 9299439]
34. el-Deiry WS et al. Topological control of p21WAF1/CIP1 expression in normal and neoplastic tissues. Cancer Res 55, 2910–2919 (1995). [PubMed: 7796420]
35. Tasic B et al. Site-specific integrase-mediated transgenesis in mice via pronuclear injection. Proceedings of the National Academy of Sciences of the United States of America 108, 7902–7907, doi:10.1073/pnas.1019507108 (2011). [PubMed: 21464299]
36. Hippenmeyer S et al. Genetic mosaic dissection of Lis1 and Ndel1 in neuronal migration. Neuron 68, 695–709, doi:10.1016/j.neuron.2010.09.027 (2010). [PubMed: 21092859]
37. Safran M et al. Mouse reporter strain for noninvasive bioluminescent imaging of cells that have undergone Cre-mediated recombination. Mol Imaging 2, 297–302 (2003). [PubMed: 14717328]
38. Tinkum KL et al. Bioluminescence imaging captures the expression and dynamics of endogenous p21 promoter activity in living mice and intact cells. Molecular and cellular biology 31, 3759–3772, doi:10.1128/MCB.05243-11 (2011). [PubMed: 21791610]
39. Schafer MJ et al. Exercise Prevents Diet-Induced Cellular Senescence in Adipose Tissue. Diabetes 65, 1606–1615, doi:10.2337/db15-0291 (2016). [PubMed: 26983960]
40. Madisen L et al. A robust and high-throughput Cre reporting and characterization system for the whole mouse brain. Nat Neurosci 13, 133–140, doi:10.1038/nn.2467 (2010). [PubMed: 20023653]
41. Wang B et al. Transplanting cells from old but not young donors causes physical dysfunction in older recipients. Aging Cell, e13106, doi:10.1111/acel.13106 (2020). [PubMed: 31971661]
42. Biran A et al. Quantitative identification of senescent cells in aging and disease. Aging Cell 16, 661–671, doi:10.1111/acel.12592 (2017). [PubMed: 28455874]
43. Freund A, Laberge RM, Demaria M & Campisi J Lamin B1 loss is a senescence-associated biomarker. Mol Biol Cell 23, 2066–2075, doi:10.1091/mbc.E11-10-0884 (2012). [PubMed: 22496421]

44. Voehringer D, Liang HE & Locksley RM Homeostasis and effector function of lymphopenia-induced “memory-like” T cells in constitutively T cell-depleted mice. J Immunol 180, 4742–4753 (2008). [PubMed: 18354198]
45. Oppenheimer NJ & Bodley JW Diphtheria toxin. Site and configuration of ADP-ribosylation of diphthamide in elongation factor 2. The Journal of biological chemistry 256, 8579–8581 (1981). [PubMed: 6267047]
46. Chien Y et al. Control of the senescence-associated secretory phenotype by NF-kappaB promotes senescence and enhances chemosensitivity. Genes Dev 25, 2125–2136, doi:10.1101/gad.17276711 (2011). [PubMed: 21979375]
47. Chen LF & Greene WC Shaping the nuclear action of NF-kappaB. Nat Rev Mol Cell Biol 5, 392–401, doi:10.1038/nrm1368 (2004). [PubMed: 15122352]
48. Heise N et al. Germinal center B cell maintenance and differentiation are controlled by distinct NF-kappaB transcription factor subunits. J Exp Med 211, 2103–2118, doi:10.1084/jem.20132613 (2014). [PubMed: 25180063]
49. Hayashi S & McMahon AP Efficient recombination in diverse tissues by a tamoxifen-inducible form of Cre: a tool for temporally regulated gene activation/inactivation in the mouse. Developmental biology 244, 305–318, doi:10.1006/dbio.2002.0597 (2002). [PubMed: 11944939]
50. Fried LP et al. The physical frailty syndrome as a transition from homeostatic symphony to cacophony. Nature Aging 1, 36–46, doi:10.1038/s43587-020-00017-z (2021). [PubMed: 34476409]
51. Fried LP et al. Frailty in older adults: evidence for a phenotype. J Gerontol A Biol Sci Med Sci 56, M146–156 (2001). [PubMed: 11253156]
52. Justice JN et al. Senolytics in idiopathic pulmonary fibrosis: Results from a first-in-human, open-label, pilot study. EBioMedicine 40, 554–563, doi:10.1016/j.ebiom.2018.12.052 (2019). [PubMed: 30616998]
53. Ovadya Y et al. Impaired immune surveillance accelerates accumulation of senescent cells and aging. Nature communications 9, 5435, doi:10.1038/s41467-018-07825-3 (2018).
54. Burd CE et al. Monitoring tumorigenesis and senescence in vivo with a p16(INK4a)-luciferase model. Cell 152, 340–351, doi:10.1016/j.cell.2012.12.010 (2013). [PubMed: 23332765]
55. Karin O, Agrawal A, Porat Z, Krizhanovsky V & Alon U Senescent cell turnover slows with age providing an explanation for the Gompertz law. Nature communications 10, 5495, doi:10.1038/s41467-019-13192-4 (2019).
56. Martin-Caballero J, Flores JM, Garcia-Palencia P & Serrano M Tumor susceptibility of p21(Waf1/Cip1)-deficient mice. Cancer Res 61, 6234–6238 (2001). [PubMed: 11507077]
57. Ohtani N et al. Visualizing the dynamics of p21(Waf1/Cip1) cyclin-dependent kinase inhibitor expression in living animals. Proceedings of the National Academy of Sciences of the United States of America 104, 15034–15039, doi:10.1073/pnas.0706949104 (2007). [PubMed: 17848507]
58. Yousefzadeh MJ et al. Fisetin is a senotherapeutic that extends health and lifespan. EBioMedicine 36, 18–28, doi:10.1016/j.ebiom.2018.09.015 (2018). [PubMed: 30279143]
59. Mao X, Fujiwara Y, Chapdelaine A, Yang H & Orkin SH Activation of EGFP expression by Cre-mediated excision in a new ROSA26 reporter mouse strain. Blood 97, 324–326 (2001). [PubMed: 11133778]
60. Xu M, Tchkonia T & Kirkland JL Perspective: Targeting the JAK/STAT pathway to fight age-related dysfunction. Pharmacol Res 111, 152–154, doi:10.1016/j.phrs.2016.05.015 (2016). [PubMed: 27241018]
61. Moiseeva O et al. Metformin inhibits the senescence-associated secretory phenotype by interfering with IKK/NF-kappaB activation. Aging Cell 12, 489–498, doi:10.1111/acel.12075 (2013). [PubMed: 23521863]
62. Martin-Montalvo A et al. Metformin improves healthspan and lifespan in mice. Nature communications 4, 2192, doi:10.1038/ncomms3192 (2013).
63. Harrison DE et al. Rapamycin fed late in life extends lifespan in genetically heterogeneous mice. Nature 460, 392–395, doi:10.1038/nature08221 (2009). [PubMed: 19587680]

64. Herranz N et al. mTOR regulates MAPKAPK2 translation to control the senescence-associated secretory phenotype. Nature cell biology 17, 1205–1217, doi:10.1038/ncb3225 (2015). [PubMed: 26280535]

65. Laberge RM et al. MTOR regulates the pro-tumorigenic senescence-associated secretory phenotype by promoting IL1A translation. Nature cell biology 17, 1049–1061, doi:10.1038/ncb3195 (2015). [PubMed: 26147250]

66. Xu M et al. Transplanted Senescent Cells Induce an Osteoarthritis-Like Condition in Mice. J Gerontol A Biol Sci Med Sci 72, 780–785, doi:10.1093/gerona/glw154 (2017). [PubMed: 27516624]

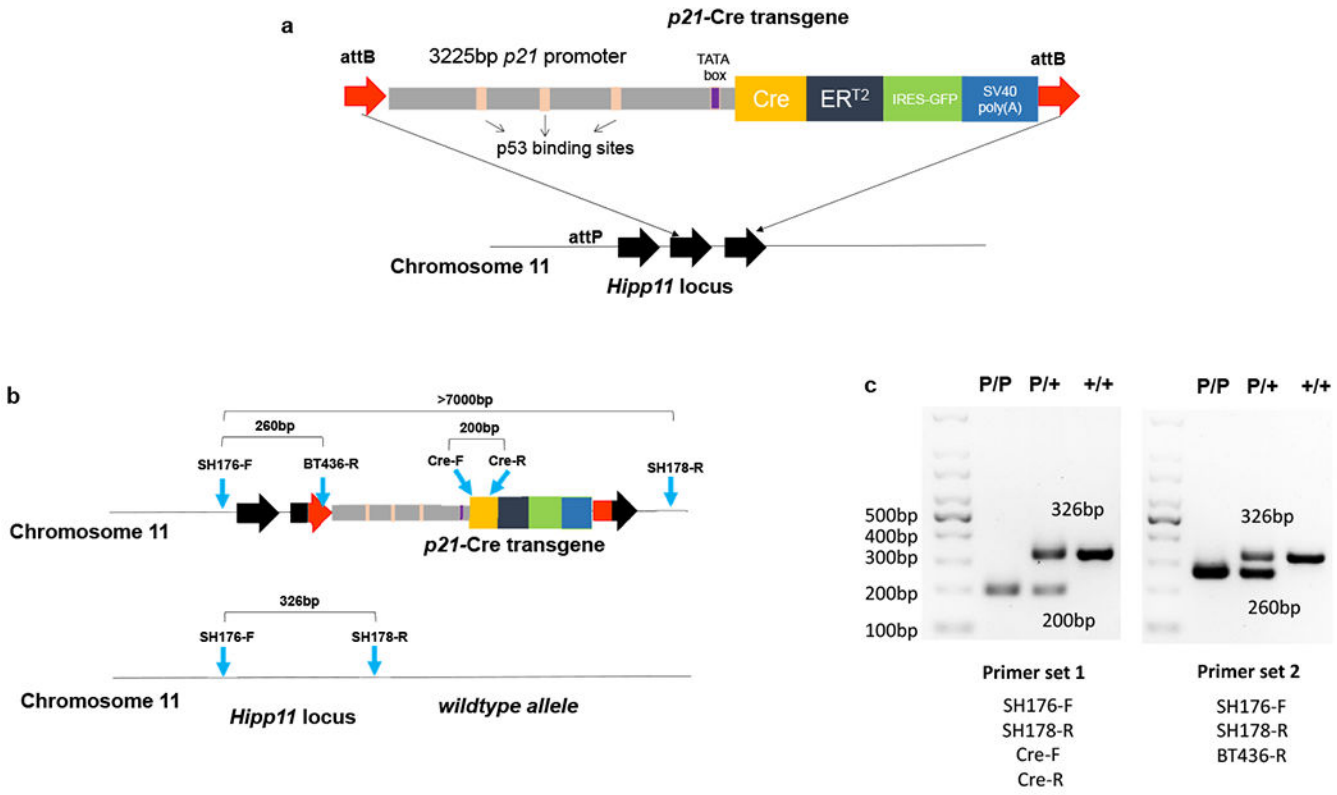

Figure 1. Generation of *p21*-Cre mouse model.

(a) Schematic of *p21*-Cre transgene. (**b**) Schematic of genotyping primers. (**c**) PCR results for two sets of genotyping primers. Set 1 was repeated in more than 2,000 mice. Set 2 was repeated in ~100 mice.

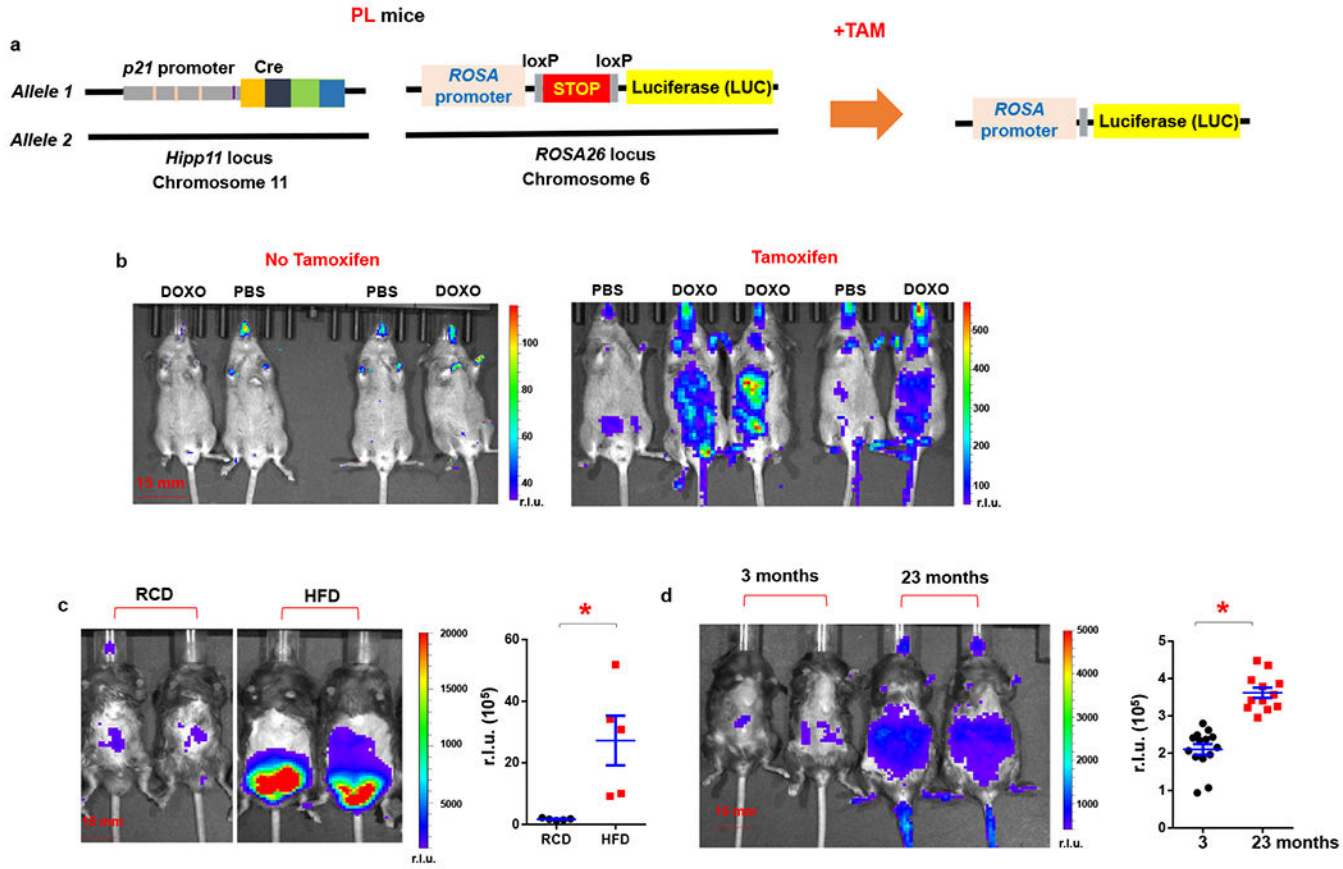

Figure 2. Whole-body live imaging of *p21*^{high} cells *in vivo* using bioluminescence imaging.

(**a**) Schematic of PL mice. (**b**) Representative images of LUC activity in DOXO or PBS treated PL mice (both male and female). Mice were given a single dose of DOXO (20 mg/kg) or PBS. Tamoxifen (2 mg/mouse) was given immediately after DOXO treatment and 16 h later, total 2 doses. BLI was performed 24 h after the DOXO administration. r.l.u., relative luciferase units. (**c**) Representative images of LUC activity in RCD or HFD-fed PL male mice, and quantification of LUC activity. n=5 for both groups. * p=0.013 (**d**) Representative images of LUC activity in young and old PL mice (both male and female), and quantification of LUC activity. n=14 for young and n=12 for old mice. Results are shown as means ± s.e.m. * p< 0.001; two-tailed, unpaired Student's t-test.

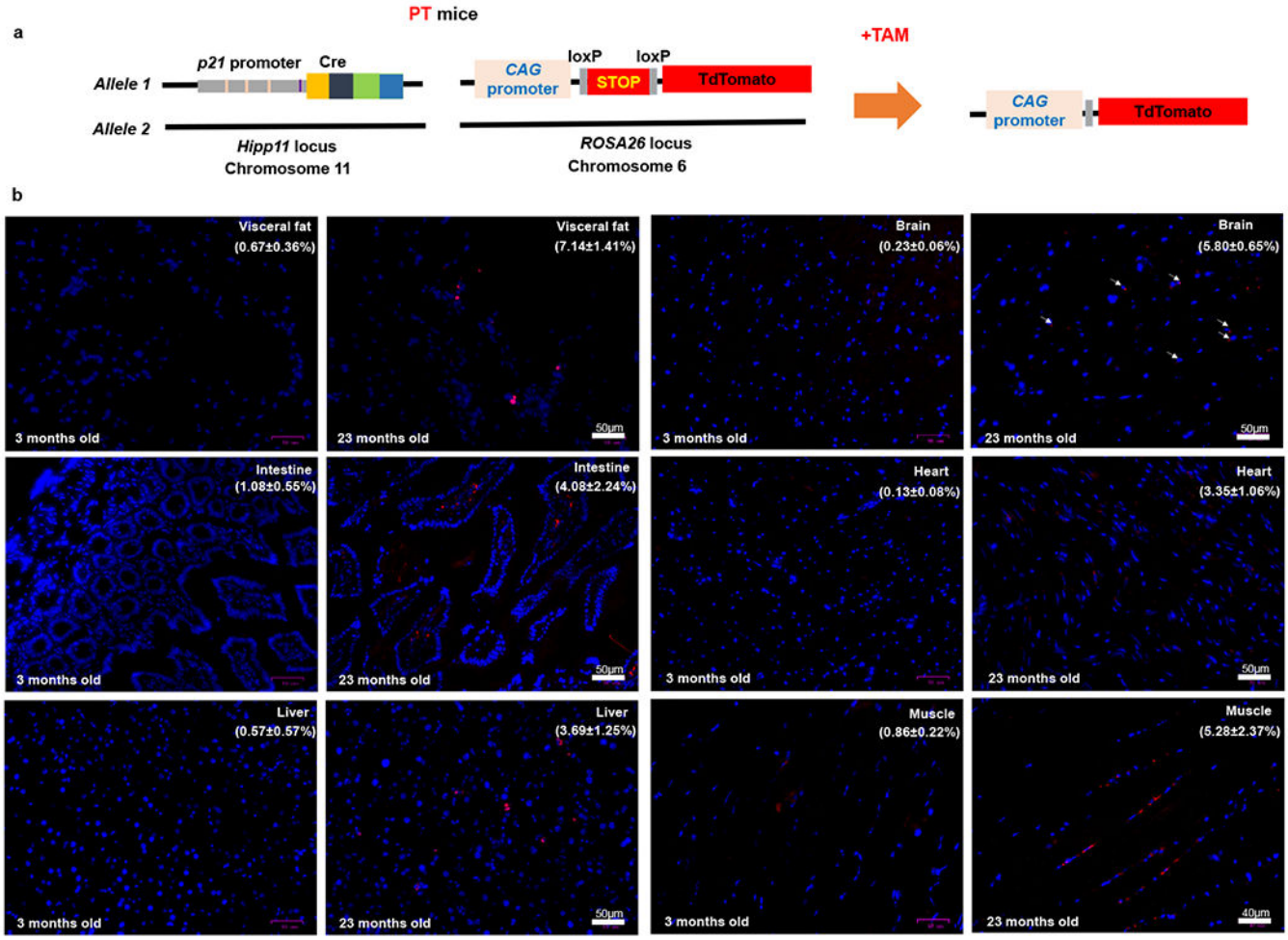

Figure 3. *p21*^{high} cells accumulate in various tissues with aging.

(a) Schematic of PT mice. (**b**) Representative micrographs of 6 tissues in young and old PT (male and female) mice. Red: tdTomato, Blue: DAPI. The percentages of tdTomato+ cells are shown as means ± s.e.m. Experiments were repeated in 3 mice.

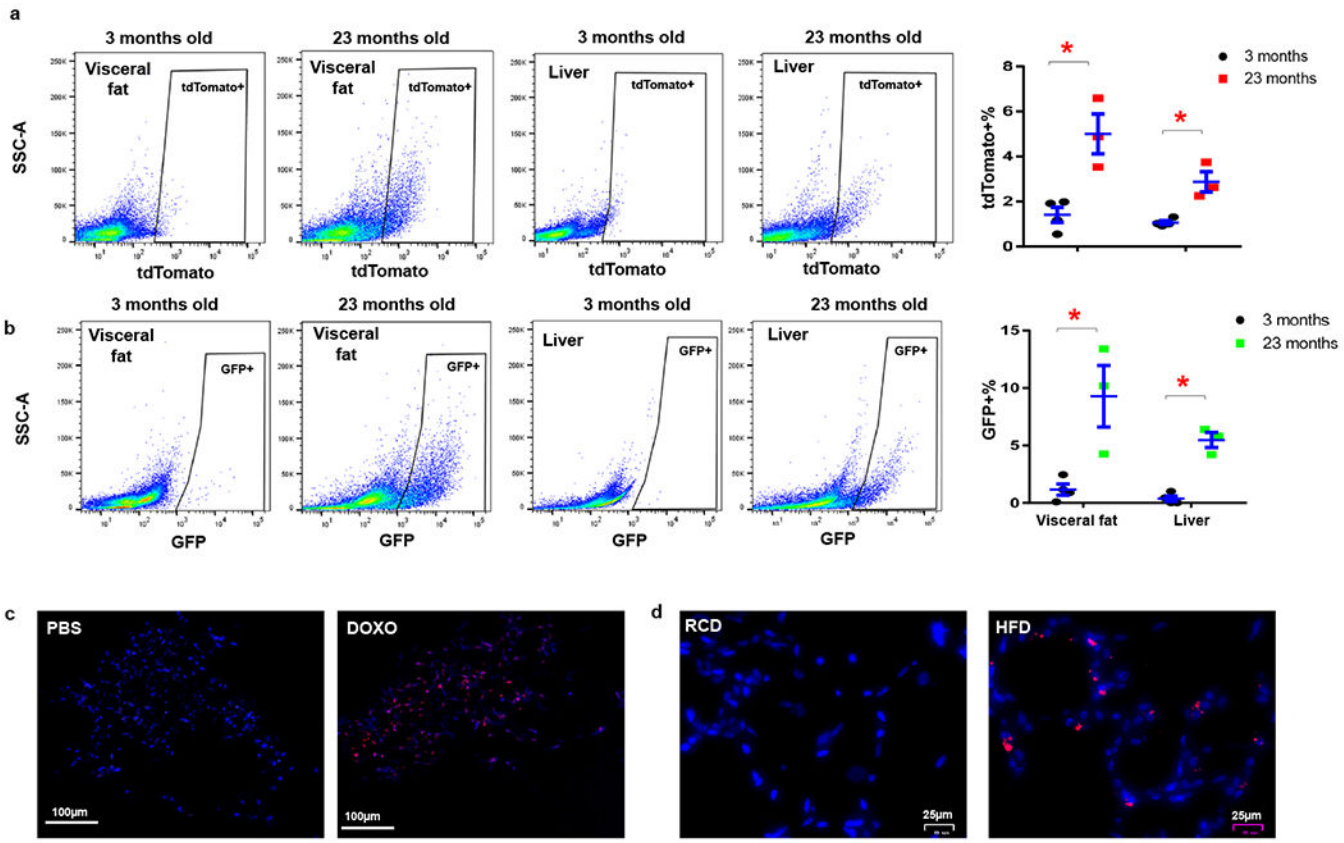

Figure 4. *p21*^{high} cells can be induced by aging, chemotherapy, and obesity.

(a) Flow cytometry analysis and proportion of tdTomato+ *p21*^{high} cells in 3-month-old (n=4) and 23-month-old (n=3) PT mice. * p=0.008 for fat, p=0.005 for liver; **(b)** Flow cytometry analysis and proportion of GFP+ *p21*^{high} cells in 3-month-old (n=4) and 23-month-old (n=3) PT mice. Results are shown as means ± s.e.m. * p=0.017 for fat, p<0.001 for liver; two-tailed, unpaired Student's t-test. **(c)** Representative micrographs of visceral fat in 3-month-old PT mice treated with PBS or DOXO. Red: tdTomato, Blue: DAPI. Experiments were repeated in 3 mice. (**d**) Representative micrographs of visceral fat in 5-month-old PT mice fed with RCD or HFD for 2 months. Red: tdTomato, Blue: DAPI. Experiments were repeated in 4 mice.

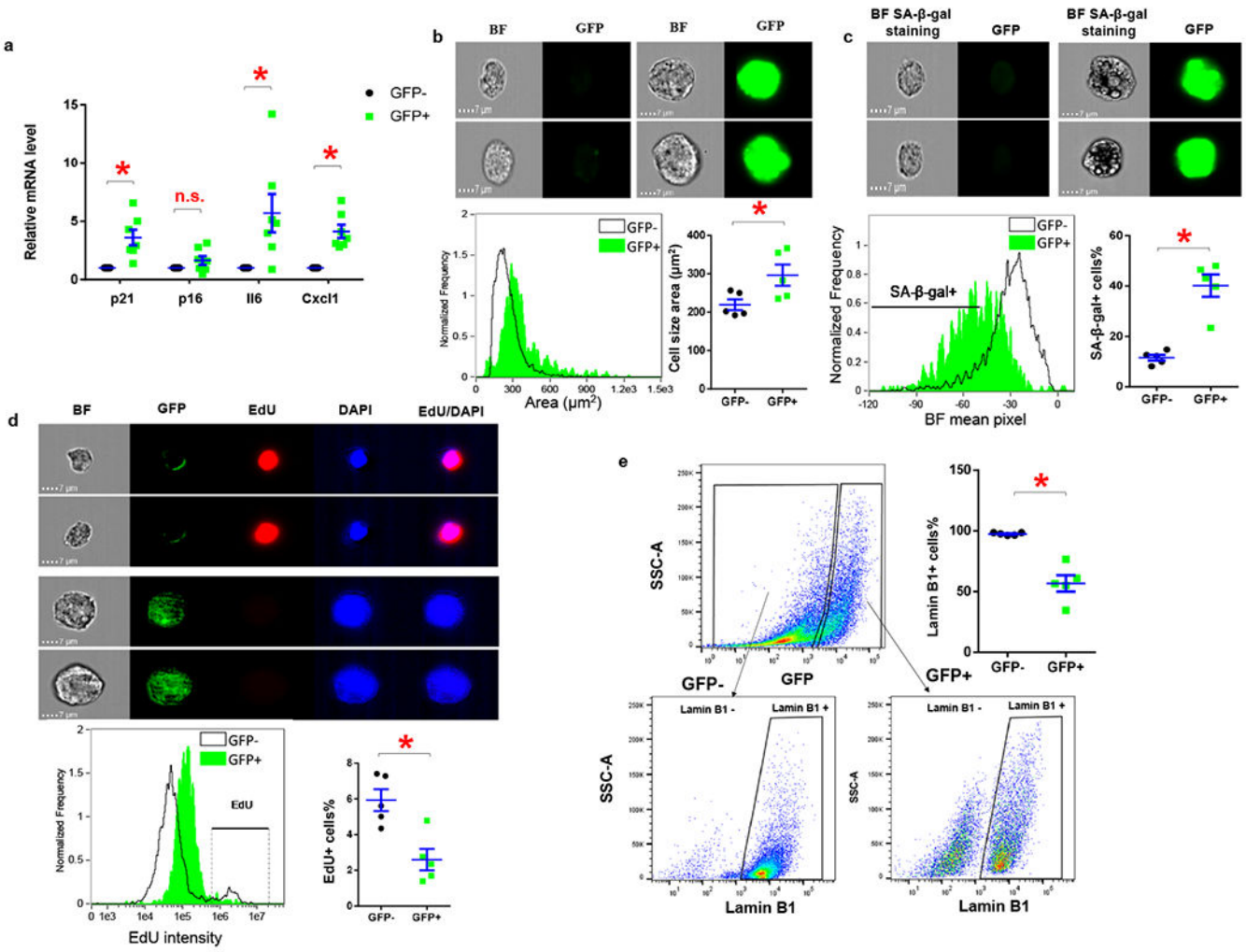

Figure 5. *p21*^{high} cells exhibit features of cellular senescence.

(a) Relative mRNA expression in GFP+ *p21*^{high} cells and GFP- cells sorted from SVF from obese PL mice. * $p< 0.05$; two-tailed, paired Student's t-test. p=0.008 for p21; p=0.1365 for p16; p=0.029 for Il6; p=0.002 for Cxcl1. **(b)** Representative images, cell size distribution and average cell size of GFP+ and GFP- cells. * p=0.006; two-tailed, paired Student's t-test. **(c)** Representative images, mean SA-β-gal staining pixel distribution, and SA-β-gal+ cells as a percentage of GFP+ and GFP- cells. * p=0.003; two-tailed, paired Student's t-test. **(d)** Representative images, mean EdU staining intensity distribution, and EdU+ cells percentage of GFP+ and GFP- cells. * p=0.019; two-tailed, paired Student's t-test. **(e)** Flow cytometry analysis of Lamin B1 in GFP+ and GFP- cells. For A, n=7 for both groups. For b-e, n=5 for both groups. Results are shown as means ± s.e.m. * p=0.004; two-tailed, paired Student's t-test.

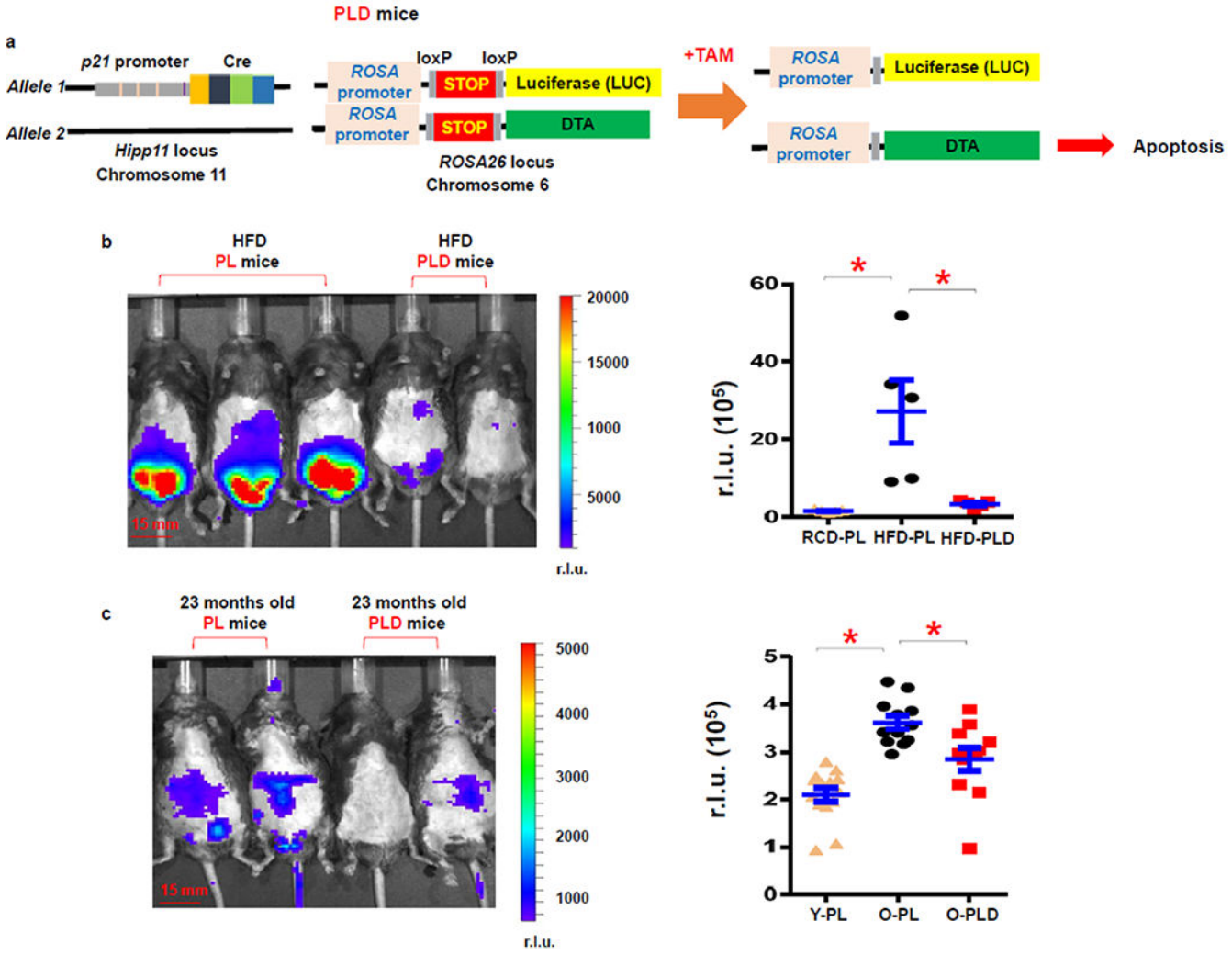

Figure 6. Inducible elimination of *p21*^{high} cells using diphtheria toxin A.

(**a**) Schematic of PLD mice. (**b**) Representative images and quantification of LUC activity in PL and PLD male mice fed with a HFD. n=5 for all groups. * $p< 0.05$; two-tailed, unpaired Student's t-test. $p=0.013$ for RCD-PL vs. HFD-PL; $p=0.018$ for HFD-PL vs. HFD-PLD. (**c**) Representative images and quantification of LUC activity in 23-month-old PL and PLD mice (both male and female). n=14 for Y-PL, n= 12 for O-PL, and n=11 for O-PLD mice. Y, young; O, old. Results are shown as means ± s.e.m. * $p< 0.05$; two-tailed, unpaired Student's t-test. $p<0.001$ for Y-PL vs. O-PL; $p=0.009$ for O-PL vs. O-PLD.

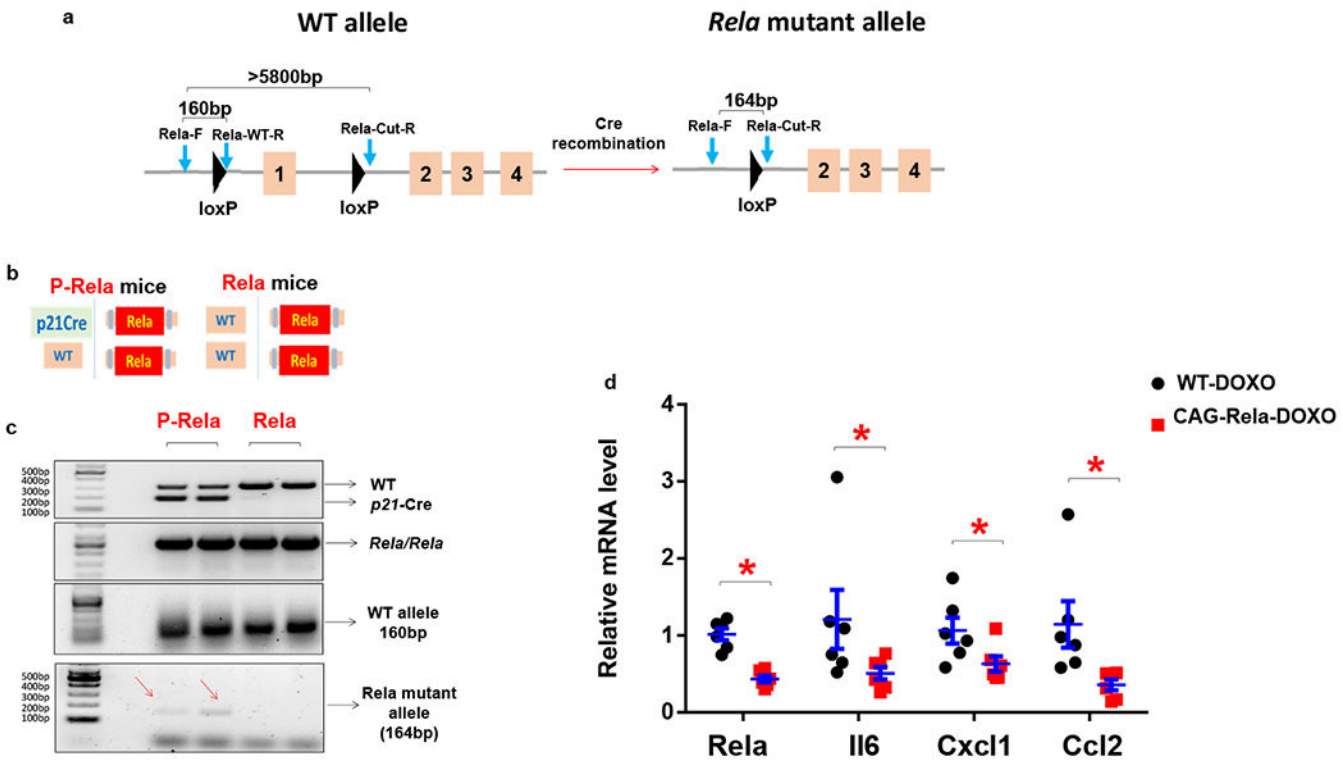

Figure 7. Genetic inhibition of SASP in *p21*^{high} cells *in vivo*.

(**a**) Schematic of floxed Rela mice. **(b)** Schematic of P-Rela and Rela mice. **(c)** PCR results using Rela-F, Rela-WT-R, Rela-Cut-R primers for SVF from P-Rela and Rela mice. Experiments were repeated in 3 mice. **(d)** Relative mRNA expression in senescent WT and CAG-Rela ear fibroblasts. n=6 for both groups. Results are shown as means ± s.e.m. * $p<0.05$; two-tailed, unpaired Student's t-test. $p<0.001$ for Rela; $p=0.037$ for Il6; $p=0.033$ for Cxcl1; $p=0.005$ for Ccl2.

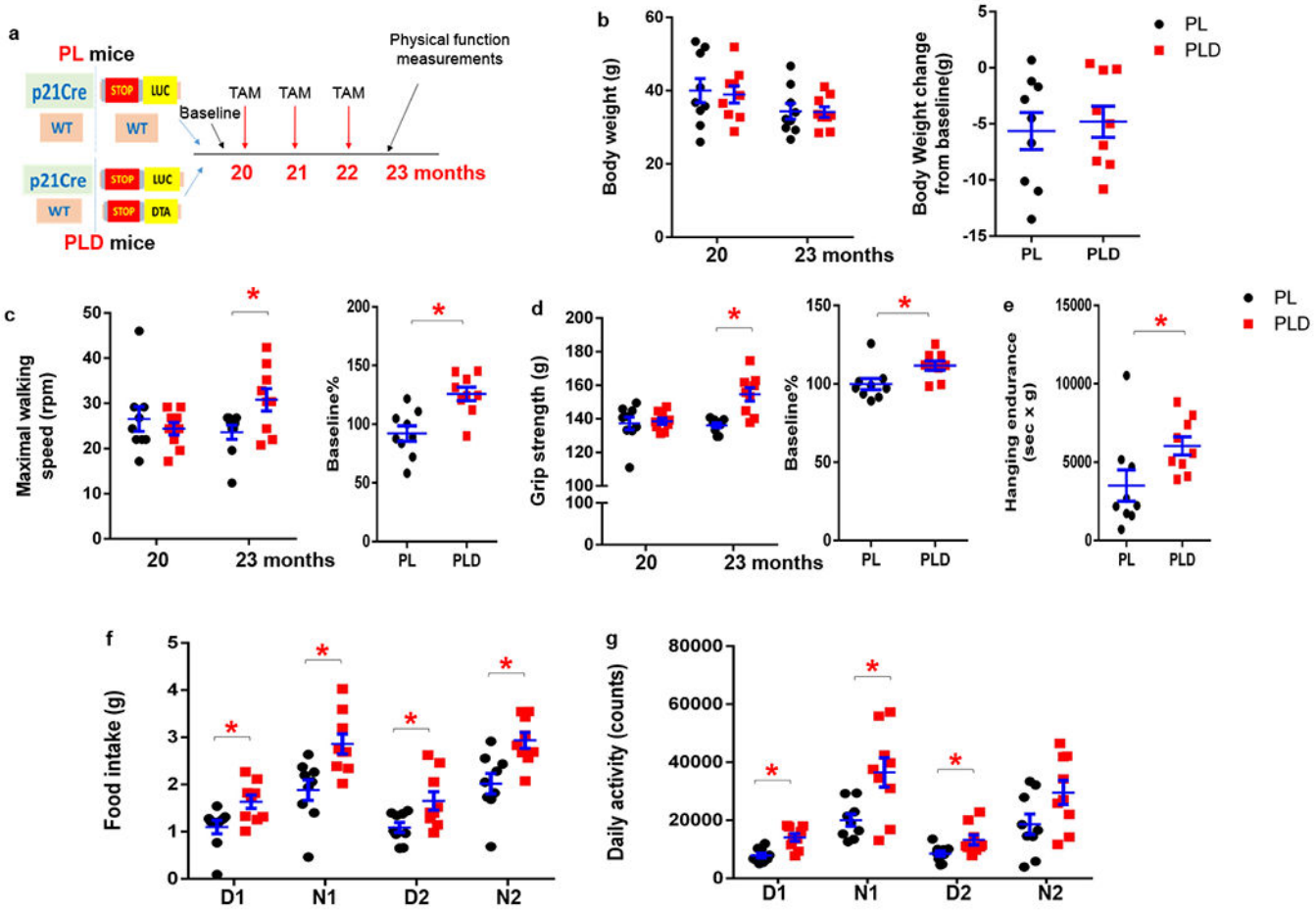

Figure 8. Clearance of *p21*^{high} cells improves physical function in old mice.

(**a**) Experimental design. **(b)** Bodyweight, **(c)** Maximal walking speed, and **(d)** Grip strength was measured in PL and PLD mice (both male and female) at age 20 months (before tamoxifen treatment) and 23 months (after tamoxifen treatment, p=). **(e)** Hanging endurance, **(f)** Food intake, and **(g)** Daily activity was measured at age 23 months. n=9 for both groups. Results are shown as means ± s.e.m. * $p< 0.05$; two-tailed, unpaired Student's t-test. For **c**, p=0.026 for 23 months; p=0.001 for baseline%. For **d**, p<0.001 for 23 months; p=0.020 for baseline%. For **e**, p=0.044. For **f**, p=0.017, 0.006, 0.022, 0.004 for D1, N1, D2, N2 respectively. For **g**, p=0.001, 0.001, 0.026, 0.062 for D1, N1, D2, N2 respectively.